

Estimating energy spectra of electron precipitation above auroral arcs from ground-based observations with radar and optics

C. Simon Wedlund,^{1,2} H. Lamy,¹ B. Gustavsson,³ T. Sergienko,⁴ and U. Brändström⁴

Received 23 January 2013; revised 16 May 2013; accepted 17 May 2013; published 17 June 2013.

[1] In 2008, coordinated radar-optical auroral observations were organized in Northern Scandinavia using the European Incoherent Scatter Radar (EISCAT) and the Auroral Large Imaging System (ALIS). A bright auroral arc was imaged on 5 March 2008 from four ground-based stations, remaining stable between 18:41 and 18:44 UT and coinciding with increased electron densities. This work presents a unified inversion framework deriving the electron energy spectrum from either optical (N_2^+ 1NG(0, 1) emission at 4278 Å) or radar (electron density) observations. An updated forward model of the ionosphere based on a 1-D kinetic Monte Carlo model is described, characterizing the linear system to invert. The 3-D blue volume emission rate is first estimated with an iterative reconstruction technique. Also presented is a novel way to calculate an accurate initial guess for auroral tomography taking into account the horizontal/vertical nonuniformity of the emission region. This technique supersedes the often-used Chapman profile as initial guess when high spatial resolution is needed. The second step, performed for the first time with ALIS optical observations, uses the forward model to retrieve from the emission rates the 2-D latitude/longitude map of the electron energy spectrum. The same model and inversion methods are finally applied to the EISCAT electron density profiles to derive the temporal energy spectrum of precipitating electrons along the magnetic zenith. Energy spectra from radar and optics are in good agreement. Results suggest that the arc is generated by a complex energy spectrum reminiscent of dispersive Alfvén waves with two main peaks (2.5, 6 keV) and a typical latitudinal width of 7.5 km.

Citation: Simon Wedlund, C., H. Lamy, B. Gustavsson, T. Sergienko, and U. Brändström (2013), Estimating energy spectra of electron precipitation above auroral arcs from ground-based observations with radar and optics, *J. Geophys. Res. Space Physics*, 118, 3672–3691, doi:10.1002/jgra.50347.

1. Introduction

[2] Discrete auroral arcs are the optical signature of electron acceleration processes in magnetospheric regions located at altitudes of several thousand kilometers.

[3] Two key issues of the complex coupling between the magnetosphere and the ionosphere are how electrons are accelerated and how they interact with the Earth's atmosphere to produce auroral structures. These problems have been discussed in several seminal papers focusing on the electrostatic generation of auroral arcs and their signature in multiple data sets [see *Borovsky*, 1993; *Frey et al.*, 2010].

[4] In order to study the acceleration mechanisms and to identify the location of the sources, accurate measurements of the energy spectra of precipitating electrons at the top of

the ionosphere and above the acceleration region are needed. Such energy spectra can be obtained in situ by using measurements from satellites flying at altitudes around 800 km in the ionosphere or at altitudes of a few thousand kilometers when the spacecraft passes through or above the acceleration region [e.g., *Marklund et al.*, 2011a, 2011b; *Haerendel et al.*, 2012]. This approach was developed in *Echim et al.* [2009] to study the formation of a stable discrete auroral arc using conjugated data from Defense Meteorological Satellite Program (DMSP) and Cluster [*Vaivads et al.*, 2003] and comparing these with a quasi-stationary magnetosphere-ionosphere (M-I) coupling model described in *Echim et al.* [2008]. In practice, satellites observe the electron spectra as a function $\phi(E, x(t), t)$ depending on the energy E and the time t as it varies along the trajectory x , which makes it difficult to unambiguously separate temporal and spatial variations.

[5] When no in situ satellite measurements are available, ground-based data can be used to retrieve energy spectra of electron precipitation above auroral arcs. Such inversion methods are based on the fact that the ionization profiles (and production of secondary electrons) depend linearly on the electron flux and energy. Two groups of methods may be highlighted.

¹Belgian Institute for Space Aeronomy, Brussels, Belgium.

²Finnish Meteorological Institute, Helsinki, Finland.

³EISCAT Scientific Association, Kiruna, Sweden.

⁴Swedish Institute of Space Physics, IRF Kiruna, Sweden.

Corresponding author: C. Simon Wedlund, Finnish Meteorological Institute, PO BOX 503, FI-00101 Helsinki, Finland.
(cyril.simon.wedlund@fmi.fi)

[6] The first group makes use of electron density profile measurements obtained by incoherent scatter radars to estimate the altitude and time variation of ionization from observed electron density profiles. It has been successfully developed over 30 years with steady improvements [e.g., *Vondrak and Baron*, 1977; *Vondrak and Sears*, 1978; *Brekke et al.*, 1989; *Osepian and Kirkwood*, 1996; *Semeter and Kamalabadi*, 2005; *Dahlgren et al.*, 2011]. With a few assumptions on the state of the thermosphere/ionosphere system, and with the help of a forward model to calculate the ionization from mono-energetic precipitation [*Rees*, 1963, 1989], one-dimensional (1-D) electron precipitation spectra can be calculated with accuracy. *Semeter and Kamalabadi* [2005] proposed an improved technique based on the maximization of the Burg entropy (called by these authors “Maximum Entropy Method” or MEM) showing that the statistical characteristics/average parameters (characteristic energy and energy flux) of the retrieved electron spectra are not significantly sensitive to the assumptions in the forward model. The limitation with this approach is that it only provides the energy spectra of electrons along one specific magnetic field line and, hence, does not provide any information on the spatial structure (latitude/longitude) of the electron precipitation.

[7] The second group of methods is based on optical observations. It relies on the inversion of altitude distributions of emissions that are excited only by electron impact, such as the first negative band of N_2^+ at 4278 Å or the O I ($^3P-^3S$) line at 8446 Å. The inversion is carried out in two steps: First, the 3-D volume emission rate of these emissions is reconstructed using tomography-like techniques such as the Multiplicative Algebraic Reconstruction Technique (MART) [e.g., *Gustavsson*, 1998, 2000; *Brändström*, 2003; *Semeter et al.*, 1999]. Subsequently, the corresponding altitude emission profiles are inverted to derive a good estimate of the 2-D distribution of electron precipitation fluxes at the origin of the emissions [e.g., *Gustavsson et al.*, 2001a]. Similar results can be obtained using the method developed for all-sky cameras (ASC) by *Janhunen* [2001] based on color ratios. For example, *Partamies et al.* [2004] performed inversions of multiwavelength all-sky camera images from the MIRACLE network (Magnetometers - Ionosphere Radars - All-sky Cameras Large Experiment) to estimate electron energy fluxes: 10–15 km resolution fluxes were compared to DMSP and the EISCAT Svalbard Radar and gave values of the same order of magnitude, promising a more systematic use of this technique in the future. However, because the inversion is performed on images from one site at a time, it is difficult to separate horizontal/vertical variations away from the magnetic zenith of the site.

[8] The objective of reconstruction methods is to obtain the most probable distribution of volume emissions given the observations and other conditions (e.g., positivity of solution, correlation between emission intensities in nearby volumes). For less ill-posed/underdetermined and smaller problems, it is possible to directly solve the maximum-likelihood estimation equations derived from a Bayesian formalism as shown by *Nygrén et al.* [1996] for 2-D auroral tomography. Generally speaking, the difficulty of the practical implementation of both methods for a wide range of auroral events, the sensitivity to initial conditions in the inversion process (issue of the initial guess for the

tomography reconstruction) and the lack of coordinated observations between different instruments have confined their use to highly constrained case studies.

[9] Recently, *Tanaka et al.* [2011] presented a feasibility study of a generalized-aurora computed tomography algorithm and strategy in the case of multi-instrumental data sets, including those of the future incoherent scatter radar EISCAT_3D, riometers, ALIS, and other auroral imagers present in the Scandinavian auroral latitudes. ALIS was shown to produce accurate reconstructions of precipitating electron fluxes for low-noise cases, while EISCAT radars, used in addition, could give significant improvements on the reconstructed flux. The study of *Tanaka et al.* [2011] showed that techniques are mature and will play an important role in the future with the advent of new 3-D-oriented radar and optical observatories.

[10] The present study, by making use of existing optical and radar facilities, is one such contribution. More precisely, it aims at unifying the inversion techniques between incoherent scatter radar and optical data sets and at characterizing for the first time with ALIS the electron precipitation energy flux above discrete auroral arcs. After describing the optical and incoherent scatter radar observations of the auroral event in section 2, a unified approach of these two inverse problems is presented in section 3, using the same energy deposition function for optical and radar inversions (section 3.1). A novel method to derive an accurate initial guess of the auroral 3-D distribution for iterative tomography-like reconstructions is also introduced in section 3.3.3. The resulting initial guess supersedes previous attempts which were event-dependent (usually based on Chapman profiles) [see *Gustavsson*, 1998; *Dahlgren et al.*, 2011] and ensures that the iterative reconstruction is correctly taking into account the latitudinal/longitudinal variation of the arc. Following these inversions, electron spectra can be consistently estimated from altitude profiles of N_2^+ 4278 Å volume emission rates and from incoherent scatter (IS) densities and are presented in section 4. Finally, a 2-D latitude/longitude map of electron precipitation above Northern Scandinavia is shown for the first time with the ALIS network.

2. Instrumentation and Observations

[11] This section describes the instrumentation used in the ALIS/EISCAT campaign that took place between 4 and 11 March 2008. The 24 h of observing time with the UHF radar were allocated under a Trans-National Access (TNA). This time was divided into five periods in order to maximize chances of clear weather conditions above most of the ALIS optical stations. This paper focuses on the bright discrete auroral arc appearing in 5 March, between around 18:40 UT and 18:55 UT.

2.1. The Auroral Large Imaging System (ALIS) Optical Observations

[12] The ALIS network consists of five ground-based stations equipped with optical high-resolution 1024 × 1024 pixel CCD cameras observing simultaneously the same volume of sky at altitudes above 80 km. With a binning of 4 × 4, the image size is 256 × 256 pixels. Each camera has an average field of view of 70°. For a detailed technical description of ALIS, the reader is referred to [*Brändström et al.*,

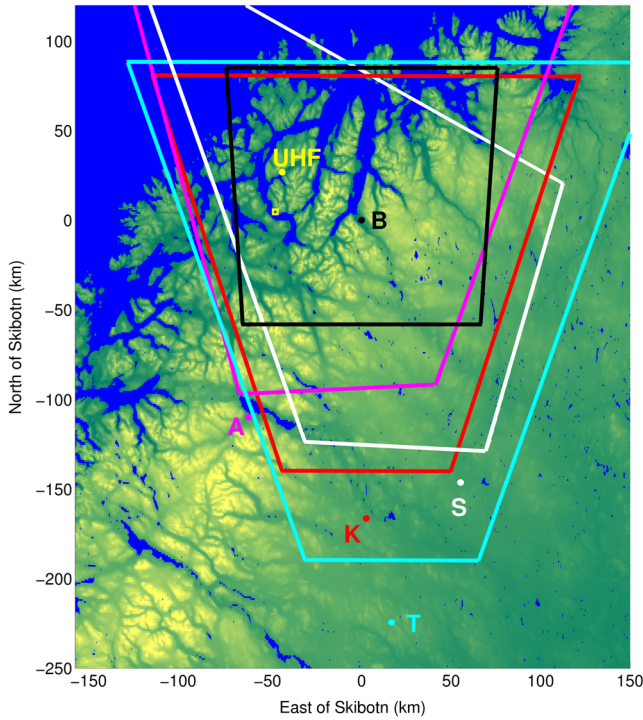


Figure 1. Map of the ALIS optical network in Northern Sweden and Norway. Shown here are the five stations Skibotn (B, black), Abisko (A, magenta), Silkkimuotka (S, white), Tjautjas (T, cyan), Kiruna (K, red). Their fields of view for the March 2008 campaign are projected onto a horizontal plane at 100 km altitude. The Skibotn camera, with a field of view of circa 90° , is looking toward zenith encompassing the EISCAT radar field of view (UHF, yellow), while the remaining stations are pointing toward this general direction.

2001] and Brändström [2003]. The network is located in the Northern part of Sweden and Norway and was designed with a mean baseline of 50 km between stations to ensure accurate tomographic reconstruction of three-dimensional volume emission rates as seen in Figure 1 [Gustavsson, 1998] but has historically been used for a wide range of studies, with or without the 3-D capability. A bibliographical account of research with the ALIS network, its uses, and applications, is attempted in Appendix A. Each station is equipped with narrow interference filters of 40 \AA width centered on the most intense auroral lines of the night spectrum, i.e., $N_2^+ 1NG (B^2 \Sigma_u^+ - X^2 \Sigma_u^+)$ 4278 \AA , $OI(^1S - ^1D)$ 5577 \AA , $OI(^1D - ^3P)$ 6300 \AA , $OI(3p^3P - 3s^3S)$ 8446 \AA , corresponding to blue, green, red, and near-IR emissions. One image is

taken approximately every 5 s by the CCD camera, including an overhead time of 1–2 s to switch filters.

[13] During the March 2008 campaign, observations were carried out with four stations, Skibotn, Silkkimuotka, Tjautjas, and Abisko. Each camera was oriented toward a common volume centered above Skibotn, at altitudes above 80 km and covering the Tromsø EISCAT UHF field of view (Figure 1). The Skibotn station is located at 69.35°N , 20.36°E , and has a 90° field of view. Table 1 summarizes the operational parameters for the four ALIS stations. ALIS was operating with a filter wheel sequence alternating between blue, green, red, and near-IR, chosen at the beginning of the auroral season to allow specific color ratios to be performed alongside tomography. It was unfortunately not identical from one station to the other. At each time step, a minimum of three stations must use the same filter to ensure tomographic reconstruction; therefore, the time resolution for tomography varied from 10 to 20 s depending on the filter sequence. This time resolution was adequate to characterize discrete auroral arcs as studied in this article but was unable to capture the features of more dynamic auroral structures.

[14] Figure 2 presents the time sequence of ALIS images recorded at the Skibotn station: A clear drift of the discrete arc from South to North directions was observed between 18:38 UT and 18:53 UT with an associated spreading in latitude. The main auroral intensification occurred between 18:41 and 18:44 UT, with the average intensity of the arc and its global morphology remaining stable. This bright episode will be the focus of the present study. Owing to their observed timescale and stability, these discrete structures may be interpreted as quasi-stationary in the sense of *Echim et al.* [2008], with a characteristic duration of 2–3 min. Accordingly, this duration is equivalent to the transit time for Alfvén waves to travel between the generator (probably located in the plasma sheet region or the plasma sheet boundary layer) and the dissipation region (the auroral arc). It is a measure of the stationarity of the entire auroral circuit including the generator and the discrete auroral arcs and may allow the application of quasi-static kinetic models to this specific episode.

[15] Figure 3 shows the four station images for the 4278 \AA and for 5577 \AA emissions at the time where the aurora was brightest, around 18:42 UT. The images of station Tjautjas, displayed in Figure 3d, exhibited an unusable area of half-circular shape due to the filter wheel being stuck in intermediate position. However, because Tjautjas is situated at the far south end of the ALIS network (see Figure 1) and because of associated perspective effects, the common volume of space imaged by ALIS was not significantly impacted by this unusable area, which was carefully removed from the reconstruction pattern. The quality of the

Table 1. Operational Parameters of the ALIS Stations Used for the Tomography-Like Reconstruction^a

Station	Latitude, Longitude ($^\circ$)	Field of View ($^\circ$)	Azimuth ($^\circ$)	Zenith Distance ($^\circ$)	(x, y) Distance to Skibotn (km)
Skibotn	69.35°N , 20.36°E	90	0.0	5.0	(0, 0)
Abisko	68.35°N , 18.82°E	60	27.9	40.0	(-63.2, -109.9)
Silkkimuotka	68.03°N , 21.69°E	60	340.0	40.0	(55.3, -146.4)
Tjautjas	67.33°N , 20.75°E	60	359.9	45.0	(16.8, -224.5)

^aThe distance to Skibotn is provided in the Cartesian (x, y, z) referential coordinate system, with Skibotn marking the origin, x being positive toward the East and y positive toward the North.

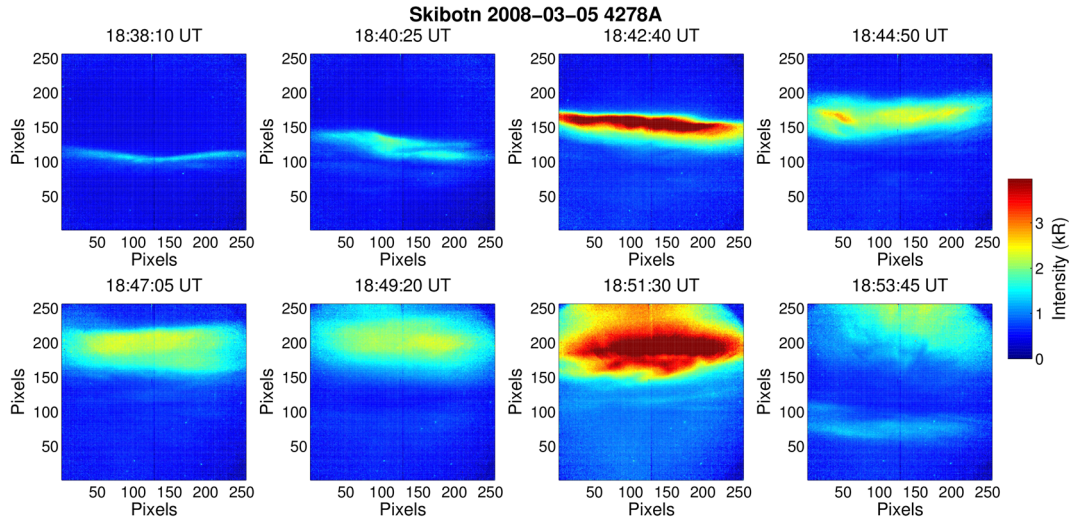


Figure 2. Calibrated ALIS 4278 Å time sequence seen from Skibotn station, between 18:38 UT and 18:54 UT. Calibration included intensity and geometry corrections. The main energizing event started around 18:41:30 and lasted until 18:44 UT included, with similar intensities. Intensities are in Rayleigh units for each emission and shown in linear scale.

data set remained good throughout the observations. The maximum of the 4278 Å emission was about 5 kR, and that of the 5577 Å was 30 kR.

[16] The arcs were clearly visible in green and blue filters with, accordingly, a higher signal-to-noise ratio for 5577 Å images than for 4278 Å images since the green line was the most intense. The overall structure of the arc was similar between green and blue filters when looking at one particular station. From the Skibotn point of view (Figure 3a), the arc was centered and seen directly overhead. It also appeared to be much thinner than from most other stations, excluding Tjautjas. When accounting for projected fields of view as in Figure 3, the images from Skibotn showed in first approximation the latitudinal/longitudinal natural spread of

the arc while those of Tjautjas showed its altitude distribution. Moreover, the arc was mostly oriented East-West when viewed from Skibotn. In both cases, the arc was estimated to be around 12 km in altitude span and 10 km in latitudinal width. With the help of 3-D reconstruction techniques, a much more accurate estimate of these features as well as their variation in space and time and with wavelength can be performed, which will be discussed in section 4.

2.2. European Incoherent Scatter Radar (EISCAT) Observations

[17] Electron density profiles were obtained using the EISCAT UHF radar located near Tromsø, Norway (latitude 69.58°N, longitude 19.23°E). The antenna beam was

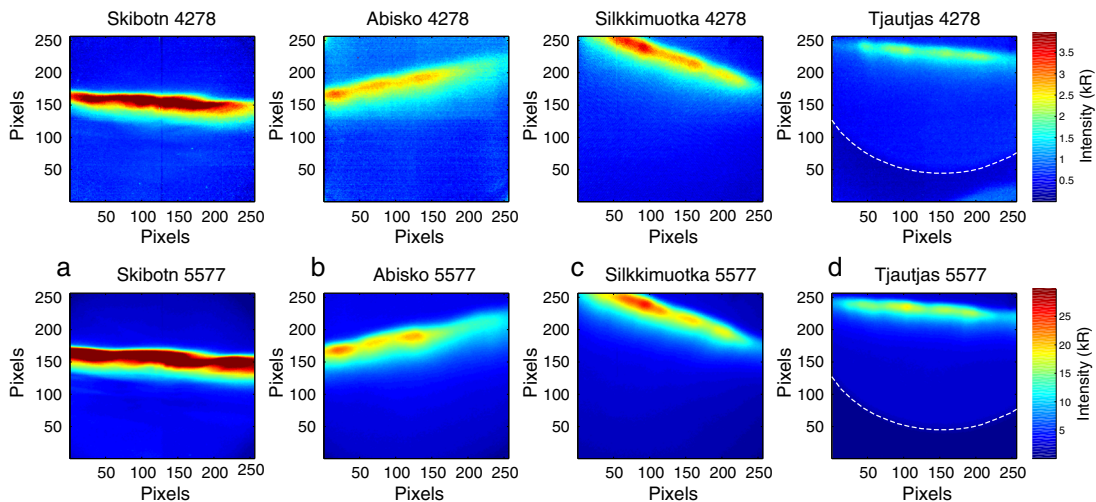


Figure 3. Calibrated ALIS (top) 4278 Å and (bottom) 5577 Å images taken at 18:42:40 UT and 18:42:45 UT, respectively. Images from four stations are shown: (a) Skibotn, (b) Abisko, (c) Silkkimuotka, and (d) Tjautjas. Intensities are in Rayleigh units for each emission and shown in linear scale. An unusable area of half-circular shape can be seen on images taken at Tjautjas and is delineated by a white dashed line. The CCD noise clearly appears on the 4278 Å images. The auroral arc was seen on all four stations.

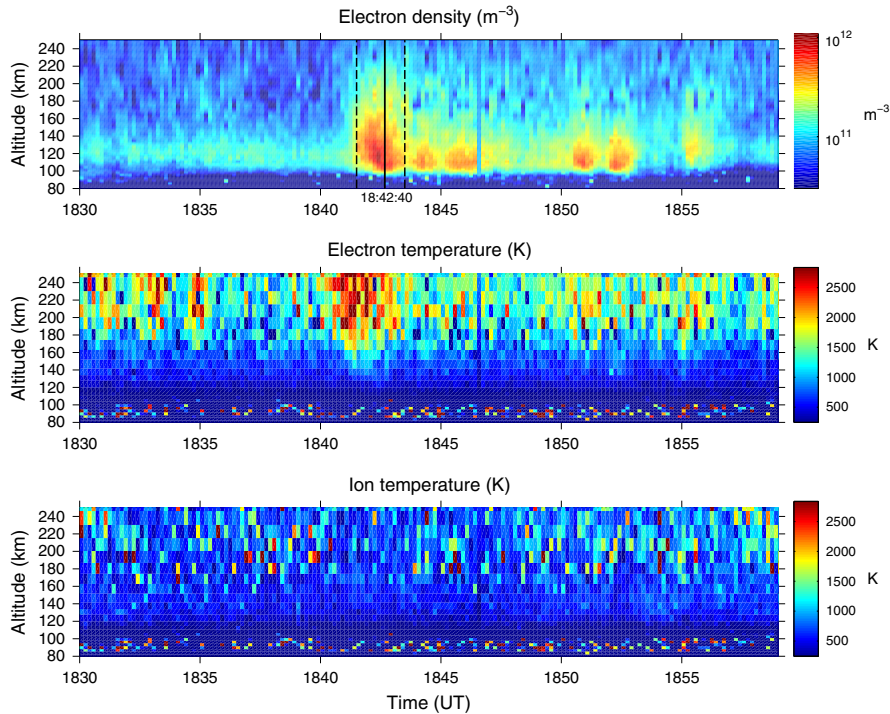


Figure 4. EISCAT UHF observations performed on 5 March 2008, between 18:30 UT and 19:00 UT, with 10 s integration time. (top) Electron densities, (middle) electron temperatures, and (bottom) ion temperatures are shown. Around 18:47 UT, a spike was seen due to a malfunction of the radar, and the analysis was unable to retrieve reliable parameters. Among the five events corresponding to crossings of the auroral arc by the radar beam, only the first one is considered in this study. The middle of the main energizing event at 18:42:40 UT is marked as a vertical black line on the density plot. Two other times (18:41:30 and 18:43:30 UT), in black dashed lines, represent the beginning and end of this event.

aligned along the magnetic field. The *beata* experiment provided an altitude resolution of $\sim 1.5\text{--}3$ km between altitudes 80 and 500 km. The raw EISCAT data were analyzed using Grand Unified Incoherent Scatter Data Analysis Program to derive ionospheric parameters with a time-integrated resolution of 10 s.

[18] Electron density profiles, as well as electron and ion temperature profiles are shown in Figure 4. Enhanced electron density profiles can be seen starting around 18:41 UT and lasting about 12 min. Typical values of the electron density peaked at $\sim 10^{12}$ m^{-3} . The spread in altitudes between 100 and 200 km at the beginning of this auroral event suggests a wide energy spectrum of the precipitating electrons. At lower altitudes, electron temperatures increased progressively with increasing altitudes with values between 500 and 1000 K. At altitudes above 180 km, they varied between 1000 and 2000 K on average but reached values of 2500–3000 K at the beginning of the event around 18:42 UT. Ion temperatures are more uniform throughout the altitude range, with values ranging from 500 K at 100–140 km altitude to 1000 K above. From the radar data, it can also be deduced that $T_e > T_i$ on the altitude span considered. If convection electric fields were present, they would produce increases in ion temperatures, resulting in the catalysis of chemical reactions involving NO^+ ions (Joule heating), which would in turn modify the structure of the electron density profile. Because such increases are not seen in the

EISCAT records, electric fields likely do not play a significant role during the duration of this event and can be safely ignored in the interpretation and inversion of EISCAT electron density profiles.

3. Data Inversion

[19] In this section, a unified inversion method for radar and optical data sets is presented. The data analysis relies on inversion techniques which can be applied to both radar and optical observations, giving a united and self-consistent picture of inverse problems. Both inverse problems take the form of Fredholm integrals of the first kind, which are then inverted with algebraic reconstruction techniques because the system of unknowns is very large. A detailed implementation of these techniques for radar and optical data is presented in the next subsections.

3.1. Forward Model

[20] The ionosphere is described by a general formalism developed for instance by Rees [1963, 1989] with updated parametrizations for the energy deposition function from *Sergienko and Ivanov* [1993]. The resulting common forward model of the ionosphere, described in detail below, is applied to the inversion of electron density profiles performed with EISCAT (section 3.2) and to the inversion of volume emission rates derived from ALIS (section 3.3).

[21] Following *Rees* [1989], the total electron production rate \mathbf{q} ($\text{cm}^{-3} \text{s}^{-1}$) can be expressed as the product between the energy deposition matrix \mathbf{A} and the flux ϕ ($\text{cm}^{-2} \text{s}^{-1} \text{eV}^{-1}$):

$$\mathbf{q} = \mathbf{A} \phi \quad (1)$$

[22] The matrix \mathbf{A} (eV cm^{-1}) contains all the physics of the degradation of electrons in the Earth's ionosphere and depends on the altitude z_i and the energy E_j . In continuous form, equation (1) can be written as a Fredholm integral of the first kind:

$$q(z) = \int_{E_{\min}}^{E_{\max}} A(z, E) \phi(E) dE \quad (2)$$

[23] In discretized form, equation (2) is simply [*Semeter and Kamalabadi*, 2005]:

$$q(z_i) = \sum_j A(z_i, E_j) \Delta E_j \phi_j(E) \quad (3)$$

with the elements of matrix \mathbf{A} defined as

$$A_{ij} = A(z_i, E_j) \Delta E_j = \frac{\Lambda \left(\frac{s(z_i)}{R(E_j)} \right) \rho(z_i) E_j (1 - \mathcal{A}(E)) \Delta E_j}{R(E_j) W(E_j)} \quad (4)$$

where:

[24] 1. ρ is the atmospheric mass density (g cm^{-3}),
 [25] 2. $s = \int_z^{\infty} \rho(z) dz$ is the scattering depth (g cm^{-2}),
 [26] 3. R is the average range of an electron in air (g cm^{-2}),
 [27] 4. Λ is the dimensionless energy dissipation function,
 [28] 5. \mathcal{A} is the dimensionless function describing the part of the total energy contained in the initial electron flux that is backscattered by the atmosphere (here seen as an albedo flux),

[29] 6. W is the average energy expended in the creation of an electron-ion pair (eV).

[30] The atmospheric mass density ρ is given by the semi-empirical model MSISE-00 [*Hedin*, 1991; *Picone et al.*, 2002] for the desired date, decimetric index $F10.7$ (in units of $10^{-22} \text{W m}^{-2} \text{Hz}^{-1}$) and planetary geomagnetic index Ap . On 5 March 2008, the solar activity was overall low with $F10.7 = 70$ and $Ap = 15$.

[31] The average energy per electron-ion pair W in air was measured at around 35 eV for electron energies above 1 keV [*International Commission on Radiation Units and Measurements Report*, 1993]. However, below ~ 150 eV, W becomes highly energy-dependent due to nonelastic collisions as pointed out by a number of authors [e.g., *Sergienko and Ivanov*, 1993; *Simon Wedlund et al.*, 2011]. The energy-dependent recommendation of *Simon Wedlund et al.* [2011] computed with their updated transport kinetic model is adopted in the present study. Following *Rees* [1989], W allows, from the total ionization rate $q(z, E)$, the computation of the energy deposition ε ($\text{eV cm}^{-3} \text{s}^{-1}$) for field-aligned monoenergetic electrons at energy E :

$$\varepsilon(z, E) = q(z, E) W(E). \quad (5)$$

[32] The expression of the range is taken from *Sergienko and Ivanov* [1993]:

$$R(E) = B_1 E^{1.67} (1 + B_2 E^{B_3}), \quad (6)$$

with E in keV. Note that values for the three coefficients B_1 , B_2 , and B_3 in Table 7 of *Sergienko and Ivanov* [1993]

Table 2. Parameters Used in the Range Calculation^a

Pitch Angle Distribution	B_1	B_2	B_3	
Monodirectional	$2.160 \cdot 10^{-6}$	$9.48 \cdot 10^{-2}$	-1.57	SI
Isotropic	$1.804 \cdot 10^{-6}$	$9.48 \cdot 10^{-2}$	-1.57	Present study
Isotropic	$1.640 \cdot 10^{-6}$	$9.48 \cdot 10^{-6}$	-1.57	SI

^aValues marked "SI" are from *Sergienko and Ivanov* [1993].

should be corrected in the isotropic case due to a typographical error. The recommended updated values are shown in Table 2 and depend on the pitch angle distribution (isotropic or monodirectional). Tests with both distributions showed that the electron densities measured by EISCAT during this event were best reproduced with monodirectional electron precipitation. This conclusion is event-dependent and should not be generalized to other events or data sets. In the present study, monodirectional pitch angle distributions are chosen.

[33] Several expressions for the energy dissipation function Λ have been derived since *Rees* [1963], following laboratory measurements, proposed the original method to reconstruct altitude profiles of known emissions. Λ is by definition:

$$\Lambda = \frac{dE/E}{ds/R}. \quad (7)$$

[34] In the present study, the approach of *Sergienko and Ivanov* [1991, 1993] was chosen as it was more accurate than that of *Rees* [1963], especially under 2 keV energy where *Barrett and Hays* [1976] measured a strong energy dependence of Λ . *Sergienko and Ivanov* [1993] used their Monte-Carlo electron transport model to parametrize Λ for mono-energetic electron beams of energies ≥ 100 eV, including backscattered energy, accounted for by these authors as an albedo flux $\mathcal{A}(E)$, for an electron source located at 700 km altitude. The parametrized form of Λ and of $\mathcal{A}(E)$ can be respectively found in equation (A2)–Table 6 and Figure 13b of *Sergienko and Ivanov* [1993].

[35] Altitude profiles of ionization rates resulting from the degradation of monoenergetic beams of electrons, of characteristic flux $10^8 \text{cm}^{-2} \text{s}^{-1} \text{eV}^{-1}$ and energies ranging between 200 eV and 10 keV are shown in Figure 5, with $\Delta E = 1$. This figure may be compared to Figure 2 of *Semeter and Kamalabadi* [2005] and Figure 3.3.3 of *Rees* [1989]: marginal differences exist, which are linked to the different parameters chosen in the present approach (neutral atmosphere, Λ and albedo effects, range, and W value).

3.2. Inversion of IS Radar Measurements

[36] Electron fluxes are derived from Incoherent Scatter electron density data by estimating the electron production rate from equation (8) and then by inverting the linear system (3).

3.2.1. From n_e to q

[37] The first step in applying the formalism detailed above to EISCAT data is to specify the link between electron densities n_e (cm^{-3}) measured by the radar and ionization

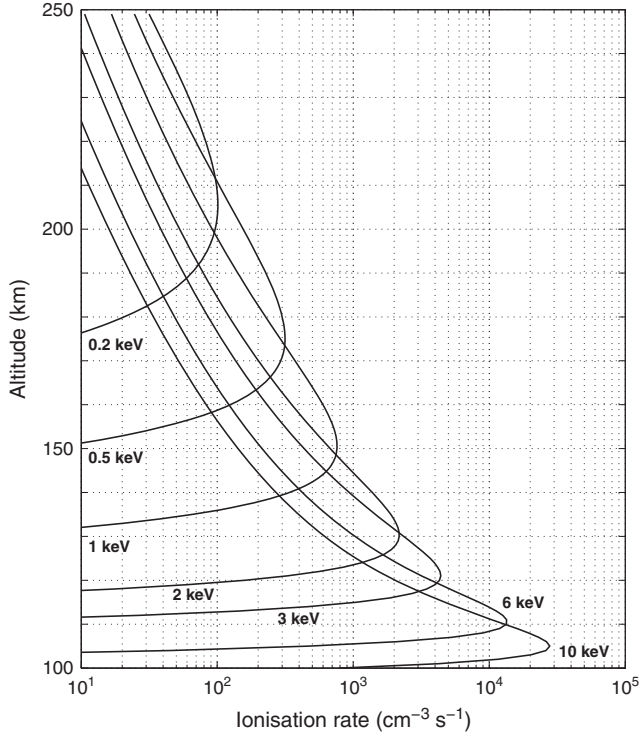


Figure 5. Ionization rates produced by monodirectional monoenergetic electrons of flux $10^8 \text{ cm}^{-2} \text{ s}^{-1} \text{ eV}^{-1}$, using the approach of *Sergienko and Ivanov* [1993]. Characteristic initial energies range between 200 eV and 10 keV.

rates q of equation (3). This is done by using the continuity equation for electrons:

$$\frac{dn_e}{dt} = q - \sum_i \alpha_i n_i n_e \quad (8)$$

[38] The α_i is the average recombination rate for ion i . To a first approximation, α is the dissociative recombination rate constant of the main ion species in the upper atmosphere, i.e., O_2^+ and NO^+ in the 100–200 km altitude range where the EISCAT UHF radar has the best signal-to-noise ratio.

[39] *Walls and Dunn* [1974] measured the cross sections for electron recombination with O_2^+ and NO^+ ions. Assuming a Maxwellian electron velocity distribution, they calculated the corresponding reaction rate constants with respect to the electron temperature. For $\text{O}_2^+ + e^- \rightarrow \text{O}_2$, *Mehr and Biondi* [1969] proposed a value of $(1.95 \pm 0.2) \times 10^{-7} \text{ cm}^3 \text{ s}^{-1}$ at $T_e = 300 \text{ K}$, later confirmed by the laboratory experiments of *Walls and Dunn* [1974]. For $\text{NO}^+ + e^- \rightarrow \text{N} + \text{O}$, *Torr et al.* [1977], using a set of in situ measurements with the Atmosphere Explorer C satellite, proposed a formula which was in agreement with the laboratory derivation of *Walls and Dunn* [1974], and was adopted in subsequent works. As demonstrated in *Walls and Dunn* [1974] and their Figures 3 and 5, both expressions are valid for electron temperatures $300 \leq T_e \leq 1200 \text{ K}$ and vary only marginally above 1200 K. These authors also pointed out that uncertainties in α_{NO^+} are much larger than in $\alpha_{\text{O}_2^+}$. From comparison with measurements, these uncertainties may be estimated at around

5% for O_2^+ and 10% for NO^+ . A 10% conservative estimate may be adopted taking into account the intrinsic uncertainty in measured electron temperatures. The O_2^+ dissociative recombination estimate of *Mehr and Biondi* [1969] was recommended by *Sheehan and St.-Maurice* [2004] after a thorough review of existing dissociative recombination rates for N_2^+ , O_2^+ , and NO^+ , where they also re-evaluated the recombination rate of NO^+ ions to be slightly slower than that of *Walls and Dunn* (1974).

[40] Following *Sheehan and St.-Maurice* [2004], the recombination rates ($\text{cm}^3 \text{ s}^{-1}$) adopted in the present study are the following:

$$\alpha_{\text{O}_2^+} = \begin{cases} 1.95 \times 10^{-7} (300/T_e)^{0.70}, & T_e < 1200 \text{ K} \\ 1.95 \times 10^{-7} (300/T_e)^{0.56}, & T_e > 1200 \text{ K} \end{cases} \quad (9)$$

$$\alpha_{\text{NO}^+} = \begin{cases} 3.50 \times 10^{-7} (300/T_e)^{0.69}, & T_e < 1200 \text{ K} \\ 3.02 \times 10^{-7} (300/T_e)^{0.56}, & T_e > 1200 \text{ K} \end{cases} \quad (10)$$

[41] T_e was taken directly from EISCAT UHF data presented in Figure 6 together with electron densities measured at 18:42:39 UT. Between 150 and 190 km altitude, sharp gradients in electron temperature were observed ranging from 800 K to 1800 K. This local structure of the ionosphere has repercussions on the altitude variation of the recombination rate and impacts the electron density profiles, with a marked change of slope above 160 km.

[42] To achieve a realistic ion composition, an averaged recombination rate coefficient may be estimated using an

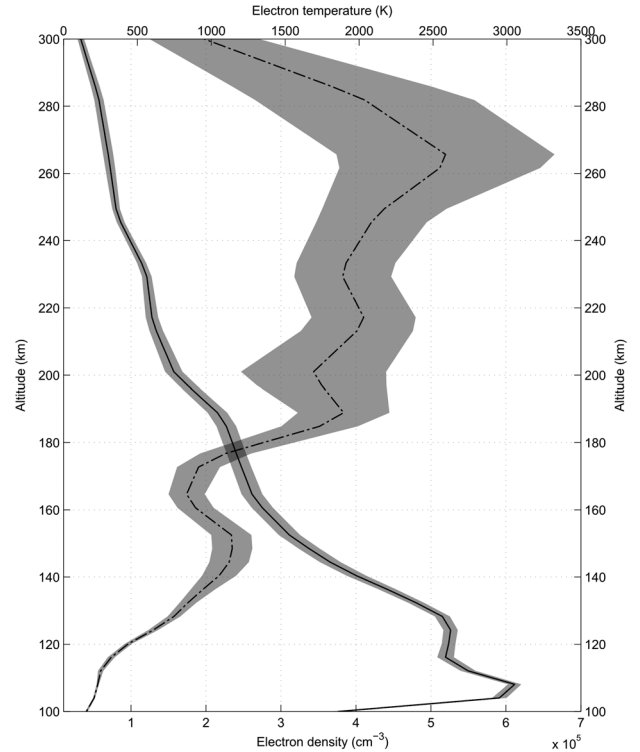


Figure 6. Example of electron density and temperature altitude profiles, here measured at 18:42:39 UT by EISCAT. Temperatures are represented by a dash-dotted line (top scale), densities by a solid line (bottom scale). Associated uncertainties are shown as a shaded confidence interval.

ionosphere model such as the International Reference Ionosphere model [e.g., *Bilitza*, 2001] or an ionospheric kinetic-fluid transport model such as TRANS4 [*Simon et al.*, 2007]. A simple bi-constituent ionosphere, made of NO^+ and O_2^+ ions, was found to be a good approximation of ion densities in the 100–250 km altitude range as modeled by the fluid part of TRANS4. In the following, we use the ratio calculated with TRANS4 and averaged over altitudes, when taking the EISCAT-retrieved electron fluxes in the middle of the arc enhancement as input to the model, so that

$$\alpha_{\text{equiv}} = (0.478 \alpha_{\text{NO}^+} + 0.373 \alpha_{\text{O}_2^+}) \equiv \alpha \quad (11)$$

is the equivalent total dissociative recombination rate for the ionosphere between 100 and 250 km altitude. The production rates including this parametrization of ion densities agree within 15% of production rates derived from a complete ionosphere, which is comparable to the uncertainty of the entire retrieval method.

[43] Because the plasma can be considered quasi-neutral ($n_i \sim n_e$) and the impinging source of electrons is assumed not to vary significantly over timescales of the order of ~ 10 s (which is the typical integration time for the UHF data to get a satisfactory signal-to-noise ratio), electron densities are close to a steady-state equilibrium, so that

$$q = \alpha n_e^2 \Leftrightarrow n_e = \sqrt{q/\alpha} \quad (12)$$

is a good approximation of the state of the ionosphere.

3.2.2. Solution of the Inverse Problem

[44] To invert this system of equations, either the multiplicative algebraic reconstruction technique (MART) or the maximum entropy method (MEM), both described in *De Pierro* [1991], may be used. Note that the MEM method of *Semeter and Kamalabadi* [2005] is referred to as the *parallel log-entropy MART* method in *De Pierro* [1991]. The nomenclature of *Semeter and Kamalabadi* [2005] as *MEM* is adopted in the following to distinguish it from the classic MART algorithm. MART converges to the solution maximizing the Shannon entropy $-\sum_j \phi_j \log \phi_j$ while MEM converges to that maximizing the Burg entropy $-\sum_j \log \phi_j$. Both approaches give fast and accurate results even in the case of data noise [*Gull and Daniell*, 1978]. *Semeter and Kamalabadi* [2005] recommended the use of MEM for IS radar data that suffer from significant uncertainties. However, it is shown here that the MART Shannon entropy maximization may be more adapted to the high signal-to-noise ratios of the EISCAT data sets.

[45] The iterative formulation of the MART method for the linear system $\mathbf{q} = \mathbf{A} \boldsymbol{\phi}$ is given by *De Pierro* [1991] and is applied here to electron densities/ionization rates q measured by Incoherent Scatter radars. Maximizing the entropy is equivalent to minimizing ϕ_j so that at the k th iteration step, with i as the altitude dimension and j as the energy dimension:

$$\phi_j^{k+1} = \phi_j^k \left(\frac{q_i^k}{\langle A_i, \phi^k \rangle} \right)^{a_{ij}} \quad (13)$$

$\langle A_i, \phi^k \rangle$ denotes the matrix multiplication of A_i , the energy deposition vector at altitude z_i , by ϕ^k (inner product). a_{ij} is the normalized (i, j) altitude/energy element of matrix \mathbf{A} , so that $0 \leq a_{ij} \leq 1$. The MEM iterative method applied to electron density data may take the form presented in *Semeter and*

Kamalabadi [2005, Appendix A] and will not be repeated here.

[46] Also following *Semeter and Kamalabadi* [2005], convergence is monitored in both methods with the help of a chi-squared test applied to the production rate uncertainty σ_q so that

$$\chi^2 = \sum_i^N \frac{|\mathbf{q} - \mathbf{A}\boldsymbol{\phi}|^2}{\sigma_q^2}. \quad (14)$$

[47] The uncertainty σ_q can be estimated from the electron density uncertainty σ_e by taking the differential of equation (12) so that $\sigma_q = \sqrt{4\alpha^2 n_e^2 \sigma_e^2 + n_e^2 \sigma_\alpha^2}$. Because EISCAT measured electron temperatures had an average uncertainty of 5% between 100 and 160 km altitude, σ_α was estimated to be of the order of 10% of α to take this effect into account (see discussion in section 3.2).

[48] The inversion method gives fast results once the energy deposition matrix (4) is calculated. Results are obtained within 5% of the original derived q for altitudes below 160 km in typically less than 300 iterations, which is determined by equation (14). A uniform flux of $1 \times 10^5 \text{ cm}^{-2} \text{ s}^{-1} \text{ eV}^{-1}$ is used as first guess of the reconstruction. The energy grid is chosen so that velocities are linearly spaced. The resolution ranges from 20 to 380 eV between 50 and 2×10^4 eV with 100 energy bins. The altitude grid is linear and spans 100 – 250 km with 1 km resolution. One inversion takes on average 8 s with these characteristics on a modern computer, easily enabling the processing of EISCAT time series.

3.2.3. Electron Flux Spectra Retrieval

[49] Figure 7 presents the inversion of the ionization rates derived from EISCAT electron densities at 18:42:39 UT, when electron densities were close to their peak value in the time series. The reconstructed differential number flux in $\text{cm}^{-2} \text{ s}^{-1} \text{ eV}^{-1}$ is shown in the left panel, when successively using the MART and MEM methods. The left panel shows the EISCAT ion production rates calculated from electron densities with expression (12) and represented by black triangles with typical error bars. The accuracy of the inversion was checked by applying the forward model to the calculated MART-derived fluxes. Excellent agreement with the derived production rates and with the observed electron densities was obtained, with a typical precision of less than 15% at all altitudes. The overall dynamics above 220 km altitude was not well captured because the assumption on the recombination was no longer valid (more atomic oxygen ions were present, participating in the chemistry of the ionosphere). Typical characteristic energies ranged between 2 and 6 keV which is consistent with the typical altitude of the electron density peaks measured by EISCAT and ranging from 110 to 130 km altitude.

[50] The MART and MEM methods yielded similar results in intensity and in characteristic energy of the precipitating electrons (main peaks at $\sim 0.7, 2.5,$ and 6 keV in Figure 7). The MEM method was found to depend more critically on the choice of the initial guess. Indeed, a severely underestimated uniform flux as initial guess in MEM, e.g., 10^3 instead of $10^5 \text{ cm}^{-2} \text{ s}^{-1} \text{ eV}^{-1}$, gave oscillations which amplified and impeded the successful convergence of the algorithm. This is due to the denominator in the MEM iterative formula becoming too small for the algorithm to

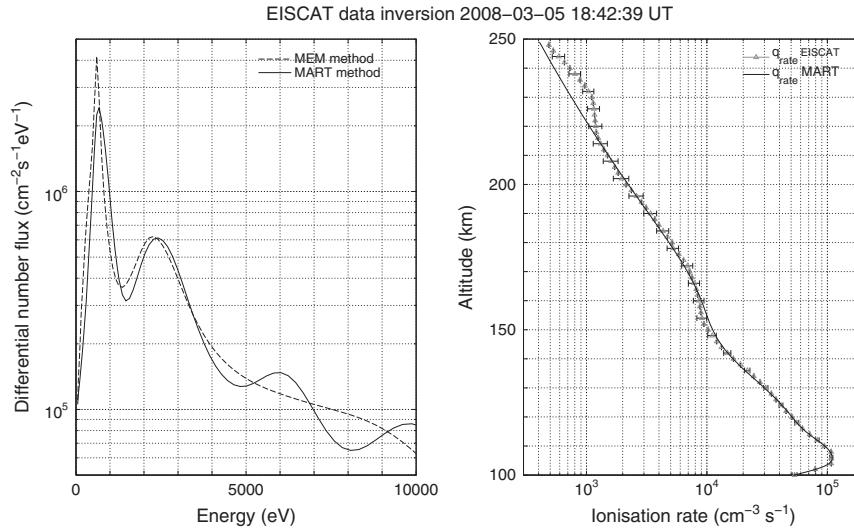


Figure 7. Inversion of EISCAT electron profiles at 18:42:39 UT. (left) Differential number flux above EISCAT reconstructed by inversion of EISCAT electron density profiles by the MART (solid line) and MEM methods (dashed line). (right) Ionization rates derived from EISCAT (black triangles) and back-projection of the MART number flux (solid line). Agreement between the two is good up to 220 km altitude.

overcome several orders of magnitude. A more “educated” initial guess is then required to fully exploit the MEM method. The MART algorithm was more accurate around the density peak (relative difference with the original density of 5%) while the MEM algorithm better reproduced the variability of the ionosphere above 160 km altitude (15% relative difference), where noise in the electron density data was more pronounced. This behavior seems to confirm the conclusions of *Semeter and Kamalabadi* [2005] that the MEM algorithm is more robust when significant noise is present. The method best suited for reconstruction of the EISCAT-derived fluxes thus depends on the ionospheric conditions and the probed region.

[51] In the following sections, the MART method was preferred for radar inversions because maximum accuracy was sought around the electron precipitation peak and for consistency between optical and radar retrievals. As explained further in section 3.3, the MART method was also used for tomography-like reconstruction of the 3-D volume emission rates.

3.3. Inversion of Optical Data

[52] The main goal of the multistation ALIS network is to determine the 3-D structure of auroral arcs. This is achieved through tomography-like reconstruction of auroral emissions from typically four stations simultaneously imaging a common volume of sky. In a second step, 2-D maps of differential electron fluxes can be obtained by inversion of the 3-D N_2^+ 1NG band volume emission rate, using the forward model and, with minor modification, the inversion technique presented in sections 3.1 and 3.2.2.

3.3.1. Principle of the Tomographic-Like Method

[53] The tomography-like method used for the ALIS cameras was presented in detail in *Gustavsson* [1998] and *Gustavsson* [2000]. A succinct summary is hereafter attempted; however, the interested reader is referred to these two works for greater depth.

[54] The 2-D intensity of each pixel in an image at one station s can be seen as a line integral of the 3-D distribution of the auroral intensity source. Following this, the forward problem may be written as a Fredholm integral of the first kind:

$$\mathbf{I}(\vec{r}_s) = \int_{\Gamma} \mathbf{K}(\vec{r}_s, \vec{r}') f(\vec{r}') d\vec{r}', \quad (15)$$

which links $\mathbf{I}(\vec{r}_s)$, the intensities in all pixels at station s , with $f(\vec{r}')$, the 3-D auroral volume emission rate. \vec{r}_s is the direction and location of the image pixels with respect to the line of sight Γ , and $d\vec{r}'$ is a differential element of position with respect to Γ . \mathbf{K} is the transfer matrix for each station that projects the 3-D source function into a 2-D image plane, taking into account all calibration characteristics. The inverse problem consists in retrieving $f(\vec{r}')$ from a set of images $\mathbf{I}(\vec{r}_s)$.

[55] In practice, the three-dimensional distribution of volume emission rates is represented with volume elements known as “blobs,” where the base-function has a 3-D cos-squared shape in x , y , and z directions. This choice gives a better representation of smooth/continuous functions than ordinary boxcar voxels [*Rydesäter and Gustavsson*, 2000]. The blobs are oriented along the local magnetic field line at the UHF radar site, assuming no curvature of the magnetic field in the reconstruction volume between 80 and 250 km altitude. On average between Kiruna and the radar site in Tromsø, the dip angle is equal to 77.2° , and the declination is 6.9° .

[56] Equation (15) then takes the form of a set of linear equations. For auroral observations with ALIS, the size of the system is $M \times N$ where M is the number of blobs (unknowns) and N is the number of pixels multiplied by the number of stations ($256 \times 256 \times 4$). In the present study, the number of blobs is $100 \times 100 \times 74$ for a typical latitude/longitude/altitude grid. This particular choice is a compromise between spatial resolution (~ 2.5 km) and

signal-to-noise ratio. Consequently, the resulting linear system of equations is underdetermined. For these values of M and N , the size of the resulting nonsquare transfer matrix \mathbf{K} is approximately $7 \cdot 10^5 \times 2 \cdot 10^5 \sim 10^{11}$ elements, which precludes direct matrix inversion. Moreover, the number of ALIS observing stations is small and since they are not uniformly distributed around the emission source, the matrix is close to singular.

[57] Therefore, iterative algebraic methods of inversion such as ART (Algebraic Reconstruction Technique), SIRT (Simultaneous Iterative Reconstruction technique) or MART (Multiplicative ART) are indicated (see the full description of the algorithms in *De Pierro* [1991]). Each of these techniques has advantages and drawbacks. While SIRT, owing to its averaging nature, is more robust to noise, MART is better at small-scale irregularities and faster in convergence. In the following, the MART procedure is chosen as a good compromise between signal-to-noise-ratio levels and swiftness in convergence.

[58] The implementation of the MART procedure consists in first starting with an initial guess f^0 for the source function, projecting it onto the first station using the matrix \mathbf{K} to yield $\mathbf{I}^0(\vec{r}_{s_1}^-)$, updating the initial guess with the ratio between the original image and the projected one, then projecting the updated source function f^1 onto the second station s_2 , and so on, until reasonable convergence is achieved. At step $q + 1$, this can be written as [e.g., *Gustavsson*, 1998]

$$f^{q+1}(\vec{r}_s) = f^q(\vec{r}_s) \cdot \frac{\mathbf{I}(\vec{r}_s)}{\mathbf{I}^q(\vec{r}_s)}. \quad (16)$$

[59] The convergence of the reconstruction is dependent on good geometry and intensity calibrations of the ALIS cameras (determination of the forward transfer matrix model \mathbf{K}), and on the quality of the initial guess, especially its altitude distribution.

3.3.2. ALIS Forward Model and Determination of the Transfer Matrix \mathbf{K}

[60] The transfer matrix \mathbf{K} includes geometry, flat field, and intensity calibrations of the CCD cameras [see *Gustavsson*, 1998, 2000].

[61] The geometry calibration provides the field of view of each pixel of each camera. A generalization of the pin-hole camera model valid for fields of view greater than 30° is used for the ALIS cameras [Gustavsson, 2000]. The field-of-view characteristics (i.e., the optical transfer function) and rotation angles of the cameras are determined by mapping the positions of stars in the images to their actual starfield positions, given by the Bright Star Catalog [e.g., *Hoffleit and Jaschek*, 1991] at the time of the observation. The geometrical part of the flat-field correction is calculated from the geometrical projection characteristics as determined from geometrical calibration done with stars found in the image data. The pixel-to-pixel photoresponse nonuniformities are very small in the ALIS cameras. In some cases, a mechanical vignetting cannot be corrected for, resulting in dark edges in some images (see Skibotn images for the wider field of view, or more critically, Tjautjas images in Figure 3).

[62] The intensity calibration is achieved using the Pulkovo Spectrophotometric Catalog of Bright Stars that gives calibrated intensities between 3200 and 10800 Å with a spectral resolution of $\sim 50\text{--}100$ Å [Aleksieva et al., 1996, 1997]. Additionally, to ensure that the resulting 3-D volume

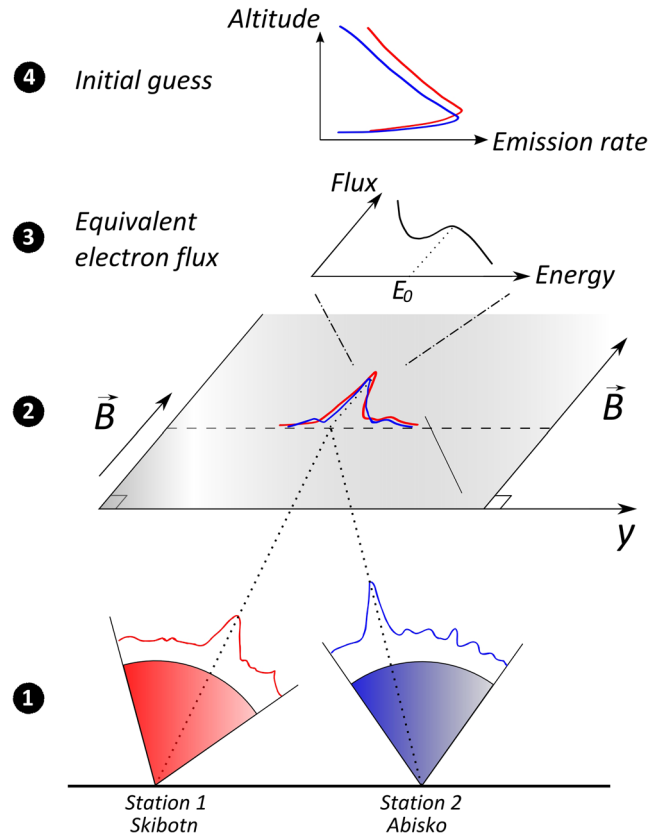


Figure 8. Principle for the determination of a tomographic initial guess in four steps. 2-D slices are projected onto a plane parallel (2) to the local magnetic field \vec{B} and intersecting the fields of view of the two stations considered, Skibotn and Abisko (1). A 2-D equivalent electron flux of characteristic energy E_0 is then obtained by comparing the resulting reconstructed intensity with intensity profiles along the magnetic zenith plane (3). Finally, the 3-D VER initial guess is obtained by applying the forward model for each block of blobs, resulting in a realistic altitude distribution (4).

emission rates (VER) intensities are consistent with those of each intensity-calibrated station, calculations of the integrated intensity in Rayleigh at the location of the origin station (Skibotn) were performed and compared to the maximum intensity along the line of sight for the original 2-D image. As a result, a scaling factor may be applied to the final VER.

3.3.3. Construction of a Physical Initial Guess

[63] To improve the quality of the 3-D reconstruction, it is beneficial to make an initial guess that is close to the true optimal distribution of the auroral arc.

[64] In a first approximation, the peak and width of the initial guess may be chosen to be uniform in latitude/longitude, a reasonable assumption for bright and stable arcs. However, over the 20 min of the auroral event studied here, electron precipitation fluxes and emission brightness were observed to vary significantly (see Figures 2 and 4), which prevented this approach from being accurate. In parallel, several altitude distributions of the initial guess were considered. A Chapman profile, assuming a single-constituent

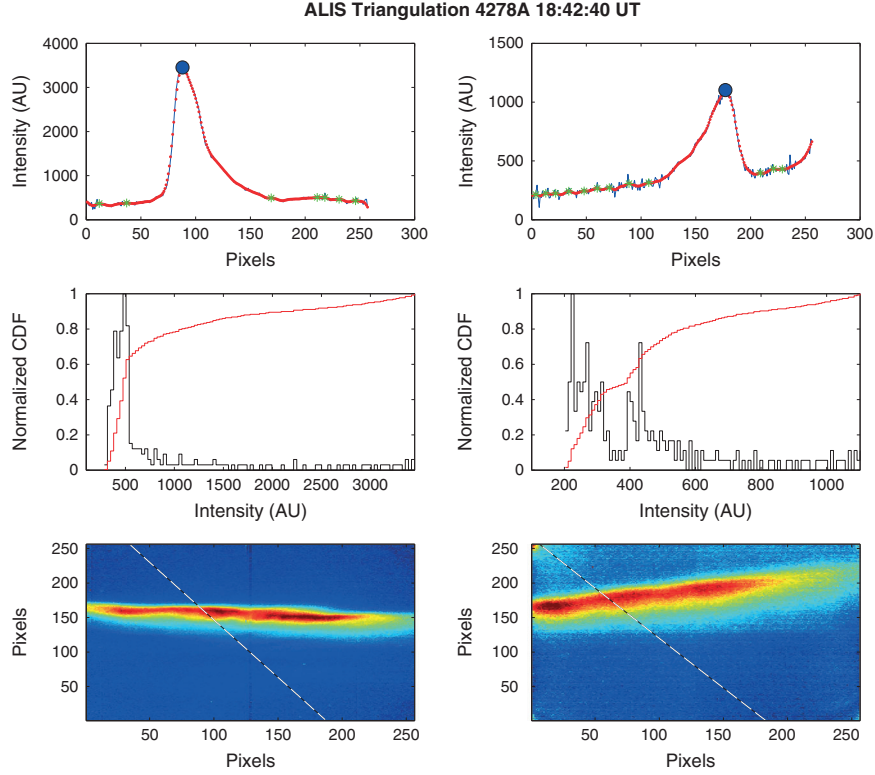


Figure 9. 1-D cuts of the 4278 Å intensity distribution for (left) Skibotn and (right) Abisko and unambiguous determination of the main peaks in each distribution at 18:42:40 UT. (top) The main peaks are drawn in blue, while the discarded minor peaks are in green. (middle) Corresponding cumulative distribution function (CDF) (red curve) and histograms of the intensity distribution (black line). (bottom) Images of Skibotn and Abisko with projection of the common projection plane along the \vec{B} -field (white dashed line).

isothermal atmosphere in hydrostatic equilibrium, is inadequate because the altitude distribution below the emission peak does not decrease fast enough, entailing inaccurate reconstructions outside the emission peak. A more realistic altitude distribution for the emissions used the dissipation function results of *Sergienko and Ivanov* [1993], as sketched out in section 3.1. A Gaussian electron flux was given as input with a characteristic energy determined by triangulating the altitude of the emission peak from two images. Because of the possible presence of multiple emission peaks in the images, the accurate identification of the same peak on several images was very difficult and could not be automated.

[65] In this section and following these first failed attempts, we describe a new method to create a good initial guess for the 3-D volume emission rate. The two-dimensional VER distribution is first estimated in the plane that intersects two ALIS stations and is parallel to the magnetic field (see Figure 8, steps 1 and 2). The altitude and longitude/latitude distribution of the volume emission is estimated by minimizing the difference between the observed image intensities along the two projections of this epipolar plane and image intensities from a modeled two-dimensional volume emission distribution in the plane, so that

$$\epsilon = \sum_{s,i} (I_s(i) - \tilde{I}(i, \vec{p}))^2 \quad (17)$$

is minimized. $I_s(i)$ and $\tilde{I}(i, \vec{p})$ are the observed and modeled image intensities at pixel i along the projection of the epipolar plane for station s , and \vec{p} are the parameters describing the electron precipitation in the plane.

[66] The volume emission rates are calculated from the forward model electron precipitation fluxes with a parameterized electron spectrum. The equivalent electron precipitation along the magnetic field in the plane is modeled with one spatially wide discrete background precipitation and one discrete precipitation for each individual local maxima (arc) in the observed epipolar image cuts. Each equivalent electron spectrum can be described by a Generalised Ellison-Ramaty (GER) distribution of the form:

$$\varphi(E) = C_0 E^{-\gamma} e^{-\left(\frac{E-E_0}{\Delta E}\right)^\kappa}, \quad (18)$$

where C_0 is a flux scaling constant and E_0 is the centered energy. γ and κ are unknowns. Note that when $\gamma = -1$ and $\kappa = 1$, the GER distribution becomes Maxwellian in energy $\propto E e^{E/\Delta E}$. The original Ellison-Ramaty distribution, used to characterize particle acceleration spectra in solar flares, is detailed in *Ellison and Ramaty* [1985]. The spectra of the discrete structures are assumed to have a Gaussian horizontal shape. This gives a model with few parameters for the two-dimensional VER in the slice having a reasonable physical altitude variation and horizontal variation that fits well to the image intensities. By minimizations of equation (17) using

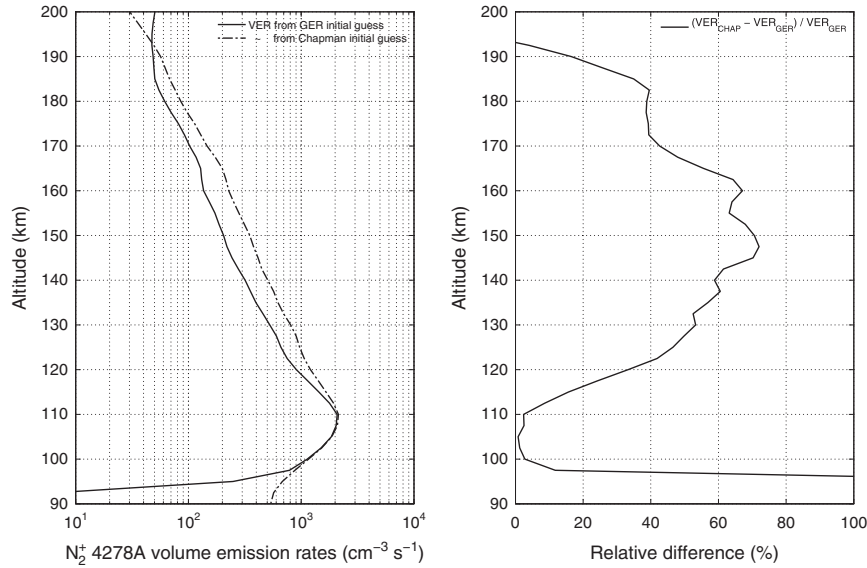


Figure 10. (left) Final volume emission rates calculated using two different initial guesses for the tomography-like reconstruction, a simple Chapman profile peaking at 110 km altitude and with a scale height of 15 km, and the new improved nonuniform initial guess (marked GER). (right) The relative difference between final VER, so that $(\eta_{\text{GER}} - \eta_{\text{Chapman}})/\eta_{\text{GER}}$.

a maximum likelihood estimator and comparison with the observed image intensities along the projection of the plane, the parameters for the position and width of the precipitation (γ_0 , $\delta\gamma$), and the electron spectrum (γ , κ , E_0 , and the flux intensity) can be determined (see Figure 8, step 3).

[67] From the two-dimensional distribution, the three-dimensional VER distribution can then be obtained by weighted extrapolation. The equivalent electron energy spectra give a good estimate of the simulated excitation/ionization profile creating the emissions (see Figure 8, step 4). The altitude and latitude/longitude variation of the initial guess of the tomography reconstruction can be evaluated by applying the forward model (described in section 3.1) to these electron spectra. Here, it is worth noting that the retrieved fluxes are not necessarily the true electron precipitation flux, especially when applying this method to emissions such as OI 6300 Å and OI 5577 Å where other factors contribute to determine the altitude profiles of the emissions.

[68] To speed up the parameter estimation, the initial guess for the horizontal position of the arcs is assumed to be located at points obtained by identifying and triangulating the local maxima of the two image-cuts along the magnetic meridian, as shown in Figure 9. Two steps are successively performed: First, 1-D cuts along the common projection plane are taken. Then, a cumulative distribution function (CDF) is derived, and peaks are singled out from the background intensity by applying a threshold of 80% intensity. From the position of these local maxima, the horizontal position and altitude of the arcs are derived, typically $z_{\text{peak}} = 110$ km for OI 5577 Å and N_2^+ 4278 Å, 120 km for OI 8446 Å, and 150 km for OI 6300 Å.

[69] This new method is quite general and, in theory, can be applied to many auroral arc cases for 3-D reconstructions. It was tested for ALIS images on the three main emissions and found to describe accurately the nonhomogeneity in latitude and longitude of the observed arcs while

giving a realistic altitude distribution for the initial guess, in agreement with profiles given by 1-D electron kinetic transport models [e.g., *Sergienko and Ivanov*, 1993; *Sergienko et al.*, 2012]. Comparison between volume emission rate profiles reconstructed using as initial guess either a uniform Chapman profile or our new technique (labeled GER) is presented in Figure 10. To reproduce at best the prevailing conditions, the Chapman profile was chosen with a triangulated peak altitude of 110 km and a scale height of 15 km. These calculations show that the VER reconstruction obtained from a triangulated Chapman profile as initial guess would be accurate only around the peak emission (less than 3% difference in VER with our general method) but significantly overestimates the VER above and below the peak (more than 60% difference). Hence, with hindsight, Chapman profiles may be realistic only at the peak emission and would only give access to the characteristic energy of the precipitation. The present method for the determination of the initial guess is shown here to successfully model the entire altitude and latitude/longitude structure of the auroral VER, giving access to the full electron energy spectrum.

[70] Once the initial guess is consistently constructed, the tomography-like reconstruction of the emissions can be performed accurately, with a good level of confidence.

3.3.4. Inversion of N_2^+ (ING) Emissions

[71] The calculation of the electron precipitation flux at the origin of auroral emissions is made possible following the approach of *Janhunen* [2001] and *Partamies et al.* [2004] for the proportionality between electron energy and emission intensity. The blue band of N_2^+ at 4278 Å is an ideal candidate, as it is only excited by electron impact and thus nearly linearly related to the incoming electron precipitation flux.

[72] *Janhunen* [2001] remarked from the theoretical and laboratory considerations of *Rees and Luckey* [1974] that, on average, the blue band emission of N_2^+ at 4278 Å emits with a rate $\zeta = 0.256$ ph keV⁻¹, allowing to link

the energy deposition (5) with the emission rate. Later, *Partamies et al.* [2004] recommended an altitude dependence of the excitation efficiency so that

$$\zeta(z) = \frac{n_{N_2}(z)}{n_{N_2}(z) + 0.7 n_{O_2}(z) + 0.4 n_O(z)} \cdot 0.628. \quad (19)$$

[73] This formulation, including the partition function for N_2 , is taken from *Sergienko and Ivanov* [1993], so that, using their energy deposition matrix, the N_2^+ ionization rate is accurately calculated. This altitude parametrization of ζ , expressed in ph keV^{-1} , is adopted in the present study. The recommendation of *Partamies et al.* [2004] is on average a factor of 2 over that of *Janhunen* [2001].

[74] Using equations (1) and (5), the blue volume emission rate η_b , in unit of $\text{cm}^{-3} \text{s}^{-1}$, is then related to the precipitation flux ϕ by the following:

$$\eta_b = \zeta \varepsilon = \mathbf{B} \phi, \quad (20)$$

with the elements of matrix \mathbf{B} (eV cm^{-1}) taking the discretized form:

$$B_{ij} = B(z_i, E_j) \Delta E_j = \frac{\zeta(z_i) \Lambda \left(\frac{s(z_i)}{R(E_j)} \right) \rho(z_i) E_j (1 - \mathcal{A}(E)) \Delta E_j}{R(E_j)}. \quad (21)$$

[75] Note that B_{ij} and A_{ij} of equation (4) are identical except in the latter for the presence of the W -value in the denominator and the absence of ζ in the numerator.

[76] Since the MART technique was chosen for the tomography-like reconstruction of the volume emission rates (VER), the inversion of the VER was performed with the MART technique as well, which algorithm is presented in section 3.2.2. Because the VER blobs are oriented along the local magnetic field line, the inversion provides physically meaningful electron precipitation fluxes.

4. Discussion

4.1. 3-D Volume Emission Rates From ALIS

[77] The 3-D reconstructed N_2^+ blue volume emission rate (VER) is shown in Figure 11 at 18:42:40 UT. A horizontal map at 110 km altitude is presented on the left panel. The auroral arc is clearly seen with fine features down to 5–10 km resolution. The width of the arc is around 10 km in latitude and mostly oriented along the West-East direction. The radar site is located at the coordinate (–44, 26) km with respect to the origin station Skibotn, situated at coordinate (0,0). The projection of the UHF beam at 110 km altitude is shown as an open circle at coordinates (–46.0, 1.9) km, at the crossing of the perpendicular white dashed lines. Along each of these lines, vertical cuts of the latitudinal and longitudinal distributions of the VER are taken, displayed on the middle and right panels, respectively. In the middle of the arc, the maximum of the emission occurs between 110 and 130 km altitude, suggesting precipitation with characteristic energies ranging from 2 to 6 keV. The auroral arc is rather homogeneous in longitude. Note that the VER unit blobs are skewed in the latitude/longitude/altitude reference system as they are oriented along the local magnetic field line.

[78] As shown in Figure 12 (left), the back-projected and original VER are within 5% of one another after inversion

between 100 and 190 km altitude. Above 190 km, the ALIS emission rate profiles exhibit a slight increase with altitude, which the inversion is not able to reproduce. This surge in emission rate may be ascribed to either secondary electrons or to an inaccurate reconstruction. Indeed, because the initial guess of the tomography-like reconstruction is typically valid below 180–200 km and the reconstruction is sensitive to initial conditions, it is difficult to validate emission rates above these altitudes. Consequently, a high level of confidence for the results is achieved between 100 and 190 km altitude.

4.2. Differential Electron Fluxes From ALIS and EISCAT

[79] Figure 12 (right) shows the electron fluxes recovered both from optical and radar observations at 18:42:40 UT. To be able to directly compare differential particle fluxes from both sources, the inversion of ALIS VER blobs was performed along the local magnetic field line corresponding to the EISCAT UHF site, hence approximately following the EISCAT UHF beam. The MART inversion technique was chosen for each, in consistency with the tomography-like reconstruction of the VER. However, the MART method is more prone to artifacts and amplifications of oscillations with increasing number of iterations [*De Pierro*, 1991], which has to be kept in mind for the interpretation. When comparing to the characteristic altitude of deposition in Figure 5, the peak altitude of the electron or emission rates seems to be driven by precipitation ranging from a few keV to about 6 keV. Hence, peaks above 8 keV are deliberately ignored in the following.

[80] Three distinct peaks can be seen, which values are presented in Table 3, together with the corresponding integrated flux values. The shape, typical values of the peaks, and energies retrieved are in reasonable agreement between the two methods. The average of the low-energy peak $\phi(E_1)$ obtained with the two methods, is found at $645 \pm 35 \text{ eV}$. This intense peak may be related to the local structure of the ionosphere around 160 km altitude with electron densities changing scale heights as a response to the strong gradients of the electron temperature, as observed by the EISCAT UHF (see Figure 6). It may also correspond to the tail of secondary electrons depositing their energy above 160 km altitude, or a combination of both mechanisms. The two high-energy peaks $\phi(E_2)$ and $\phi(E_3)$ around 2 and 6 keV (corresponding to altitudes of 120 and 110 km, respectively) are reasonably well retrieved with both data sets, with commensurate flux intensities. They are the signature of the electron precipitation event and condition the shape and main altitude distribution of electron densities.

[81] The characteristic energy of a precipitation spectrum is defined as the energy corresponding to the maximum of the differential energy flux $\phi_E(E)$ above 500–600 eV energy, the threshold below which secondary electrons play the most important role [*Semeter and Kamalabadi*, 2005]:

$$E_0 = \arg \max_{E_j} (\phi_E(E_j) \mid E_j > 500 \text{ eV}), \quad (22)$$

with the differential energy flux expressed in $\text{eV cm}^{-2} \text{s}^{-1} \text{eV}^{-1}$ and defined as

$$\phi_E(E) = E \cdot \phi(E). \quad (23)$$

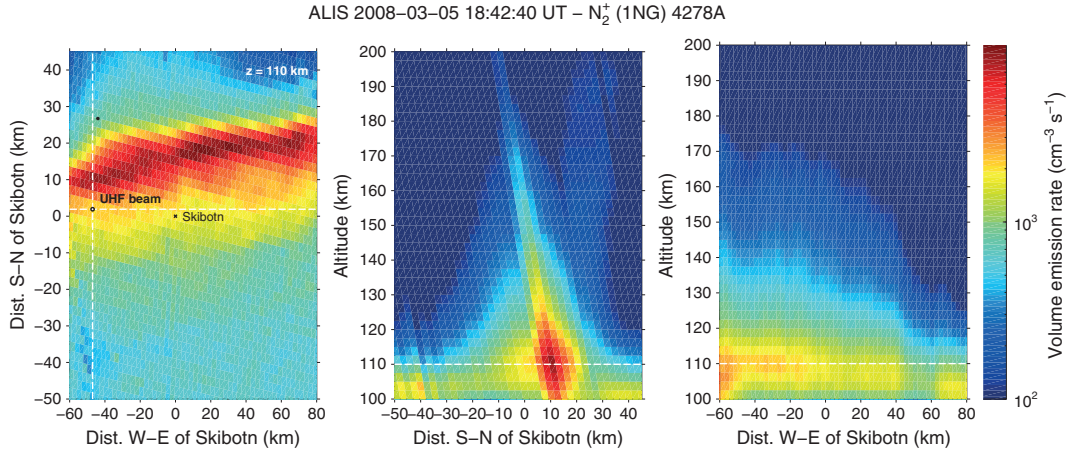


Figure 11. Planar projections of the ALIS 3-D reconstructed Volume Emission Rates at 18:42:40 UT, N_2^+ (1NG) 4278 Å emission. (left) Altitude projection at 110 km altitude in the latitude/longitude plane. (middle) Latitudinal projection versus altitude in the plane passing through the EISCAT radar. (right) Longitudinal projection versus altitude in the plane passing through the EISCAT radar. The black circle at the intersection of the two white lines on the left panel marks the location of the UHF radar field of view at 110 km altitude. The corresponding geographic location of EISCAT is marked as a black star. On the middle and right panels, the horizontal white lines represent the cut at 110 km altitude.

[82] With these definitions, three peaks are still found, but shifted somewhat in energy. The calculated characteristic energies are $E_0 = 2155$ eV (ALIS) and $E_0 = 2550$ eV (EISCAT) for the second peak and $E_0 = 5820$ eV (ALIS) to $E_0 = 6240$ eV (EISCAT) for the third peak. Differences in particle flux values between the two reconstructions may be significant at a given energy, as shown in Table 3. However, the total integrated particle fluxes Φ in $\text{cm}^{-2} \text{s}^{-1}$ defined as

$$\Phi = \int_0^{\infty} \phi(E) dE \quad (24)$$

were found to be within 2% of one another, indicating that both retrievals are in excellent agreement for integrated quantities.

[83] From successive inversions of the N_2^+ 3-D VER, a 2-D map of electron precipitation fluxes can be retrieved. Results are shown in Figure 13. The left panel displays the horizontal latitude/longitude map of electron precipitation fluxes chosen at 6 keV, and corresponding to the higher energy peak of the precipitation. The middle and right panels show, respectively, the latitudinal and longitudinal

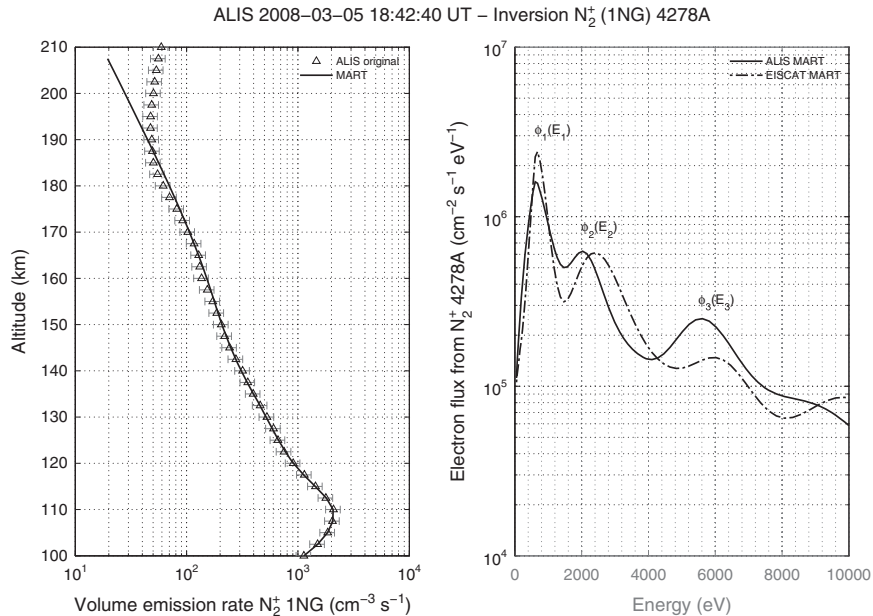


Figure 12. MART inversion of the N_2^+ blue volume emission rates reconstructed from ALIS at 18:42:40 UT. (left) Uncertainties on the ALIS emission rates are set at 15%. (right) The corresponding reconstructed flux from ALIS with MART (solid line) and from EISCAT (dash-dotted line). Local maxima $\phi(E_x)$ are highlighted and numbered.

Table 3. Comparison of the Main Characteristics of ALIS- and EISCAT-Retrieved Fluxes at 18:42:40 UT^a

	E_1 (eV)	ϕ_1 ($\text{cm}^{-2}\text{s}^{-1}\text{eV}^{-1}$)	E_2 (eV)	ϕ_2 ($\text{cm}^{-2}\text{s}^{-1}\text{eV}^{-1}$)	E_3 (eV)	ϕ_3 ($\text{cm}^{-2}\text{s}^{-1}\text{eV}^{-1}$)	Φ ($\text{cm}^{-2}\text{s}^{-1}$)	Φ_E (mW m^{-2})
ALIS	610	1.6×10^6	2030	6.3×10^5	5620	2.5×10^5	3.16×10^9	18.4
EISCAT	680	2.4×10^6	2415	6.1×10^5	6030	1.5×10^5	3.20×10^9	17.7

^a E_x is the energy at different local maxima of flux ϕ_x , as shown in Figure 12. The total integrated particle flux Φ and the net energy flux Φ_E are also given for each reconstruction. ALIS fluxes are taken at the location of EISCAT for comparison.

projections of the fluxes in the planes intersecting the EISCAT radars. A complex energy structure can be seen with multiple energy peaks at the location of the arc. As previously pointed out for the VER, the precipitation fluxes exhibit a rather homogeneous behavior in longitude.

[84] Several mitigating factors may make the comparison difficult and explain the observed discrepancies, especially in flux intensity. One factor is the relative resolutions of the grid at a given altitude, since the measurements are integrated on this projected surface. The area of the ALIS blobs is typically $2.5 \times 2.5 = 6.25 \text{ km}^2$. At 110 km altitude, the 0.6° half-beam width of the UHF radar gives a radius of the beam of the order of 1.15 km. The corresponding area of the UHF beam is then 4.17 km^2 , which is about 60% smaller than the ALIS blob surface at the same altitude. A systematic overestimate of the fluxes by ALIS with respect to the UHF radar would result, which would be greater at lower altitudes and higher characteristic energy of the precipitation. A qualitatively similar trend can be seen in Figure 12 (right panel).

[85] Another factor affecting the results at low energy may stem from the nature of the two retrieval methods. Indeed, low-energy peaks seen in the EISCAT-derived fluxes may be strongly affected by the local altitude structure of the electron density and temperature profiles, especially above 160 km altitude where uncertainties maximize. Furthermore, the assumption that the ionosphere can be represented by a unique recombination rate is only valid below about 160 km altitude. Because of this, the MEM/MART algorithms were found to be accurate above approximately

500 eV energy. Regarding the optical retrieval method, the ALIS-derived flux suffers from uncertainties in the initial guess of the tomography and assumptions on the excitation efficiency.

[86] Following this discussion, the relatively good agreement between EISCAT and ALIS-derived fluxes both for the characteristic energy and magnitude of the precipitation gives confidence in the two-step ALIS inversion, first from 2-D images to 3-D VER and then from VER to precipitation fluxes.

[87] The inversion method can be applied to the entire time sequence of 4278 \AA images from ALIS and similarly to that of electron density data from EISCAT. During this campaign, the temporal resolution for ALIS was of the order of 20 s and equal to 10 s for EISCAT to achieve an adequate S/N ratio. Figure 14 presents the electron particle fluxes from ALIS at three different stages of the main energizing event, i.e., at 18:41:30 UT (onset), 18:43:40 UT (middle), and 18:43:30 UT (end). At the onset of the event, peak energies range between 1 and 2 keV (dashed line) with no high-energy peak. During the event (solid line), high-energy precipitation appears around 6 keV and contributes to the bulk of the energy contained in the spectra. At the end of the event (stars), the high-energy peak is still present but somewhat damped in intensity while, simultaneously, the second peak around 2.5 keV is enhanced by the same amount. This transfer of net energy from the high-energy peak of the distribution to lower energies is in agreement with the temporal sequence of reconstructed spectra obtained from EISCAT measurements.

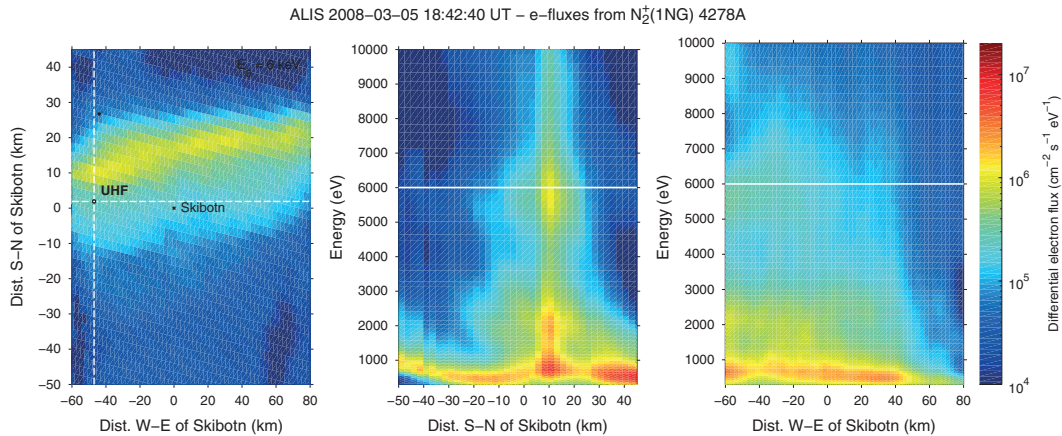


Figure 13. 2-D electron precipitation flux maps over ALIS at 18:42:40 UT, retrieved from inversions of the N_2^+ (1NG) 4278 \AA 3-D volume emission rates. (left) Energy projection at 6 keV ($\sim 110 \text{ km}$ altitude) in the latitude/longitude plane above EISCAT/ALIS. (middle) Latitudinal projection of fluxes versus energy in the plane passing through the EISCAT radar. (right) Longitudinal projection of fluxes versus energy in the plane passing through the EISCAT radar. See Figure 11 for complementary legend.

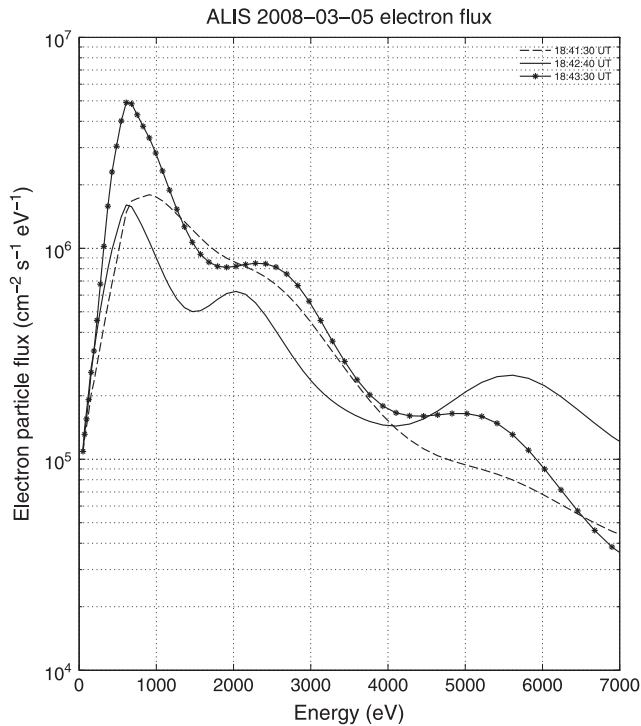


Figure 14. Electron particle fluxes retrieved with ALIS (MART inversion method) at three different stages of the main energizing event and at the EISCAT UHF location: 18:41:30 UT, 18:42:40 UT, and 18:43:30 UT.

[88] Figure 15 shows such an EISCAT sequence using the MART method as the reconstruction algorithm, at 10 s resolution. Characteristic energies typically range from to 2 keV before the auroral onset to 2.5–6 keV when bright arcs are forming. The spread in energies is maximum between 18:41:30 and 18:44:00 UT, which is correlated with higher electron densities and brighter auroral features. This spread in energy is not characteristic of the monoenergetic-dominated aurora (traditionally labeled “inverted V”) associated with acceleration by quasi-static parallel electric fields. Rather, this behavior suggests a wave-dominated aurora with a broadband acceleration mechanism due to

dispersive Alfvén waves (DAWs), typically observed by spacecraft such as the DMSP satellites [Chaston *et al.*, 2007; Newell *et al.*, 2009]. Despite the observed stable character of the auroral arc in terms of intensity and dynamics, it is therefore not clear whether it can be associated with an acceleration mechanism due to a quasi-stationary parallel electric field.

4.3. 2-D Energy Flux Maps and Radar-Optics Comparison

[89] A convenient way to present the 2-D electron fluxes retrieved from ALIS is to calculate the total integrated energy flux, or net energy flux, along each magnetic field line. Note that the spatial coordinates for the net energy flux correspond to the highest altitude of the reconstruction grid, here 260 km altitude.

[90] The net energy flux Φ_E , expressed in mW m^{-2} , is a crucial parameter of magnetosphere-ionosphere coupling models such as that of Chiu and Cornwall [1980], Lyons [1981], Janhunen and Huuskonen [1993], or Echim *et al.* [2008]:

$$\Phi_E = \int_0^{\infty} E \phi(E) dE. \quad (25)$$

[91] The net energy flux at 18:42:40 UT derived from EISCAT is found equal to 17.7 mW m^{-2} while the ALIS-derived net energy flux along the same field line is 18.4 mW m^{-2} , a difference of less than 4%. The net energy fluxes at the onset (18:41:30 UT) and at the end of the main event (18:43:30 UT), corresponding to particle fluxes shown in Figure 14, are equal to 15.0 and 17.5 mW m^{-2} , respectively.

[92] A latitude-longitude energy flux map at 18:42:40 UT is presented in Figure 16 at 260 km altitude, together with the cut across the arc intersecting the EISCAT location. Note that because the deposited energy flux follows the local magnetic field line, the arc appears to be shifted southward with respect to the image shown in Figure 13. The position and corresponding value of the EISCAT-retrieved energy fluxes are shown. In the middle of the arc (Figure 16, top panel), the net energy flux ranges between 60 and 80 mW m^{-2} . Along the meridian passing by the EISCAT UHF location (bottom panel), the arc width is found equal to 7.5 km , measured by the full width at half maximum of a fitted Gaussian distribution, which is in agreement with estimates from the VER

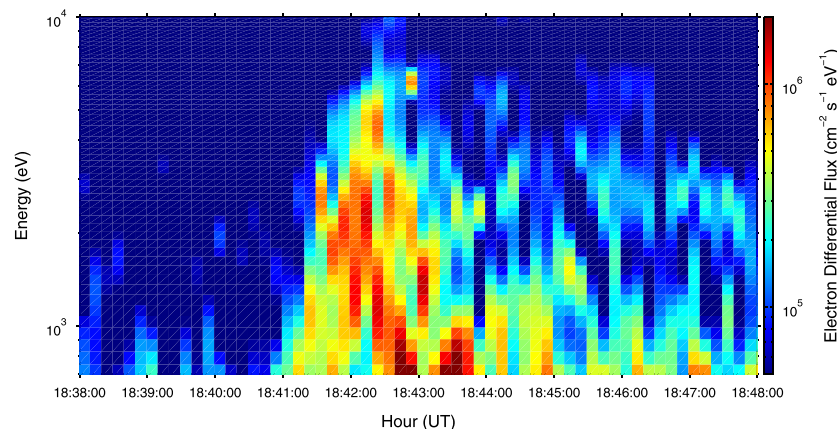


Figure 15. Time series of the 10 s electron precipitation fluxes reconstructed from EISCAT UHF observations, 5 March 2008 18:38–18:50 UT, by the MART method.

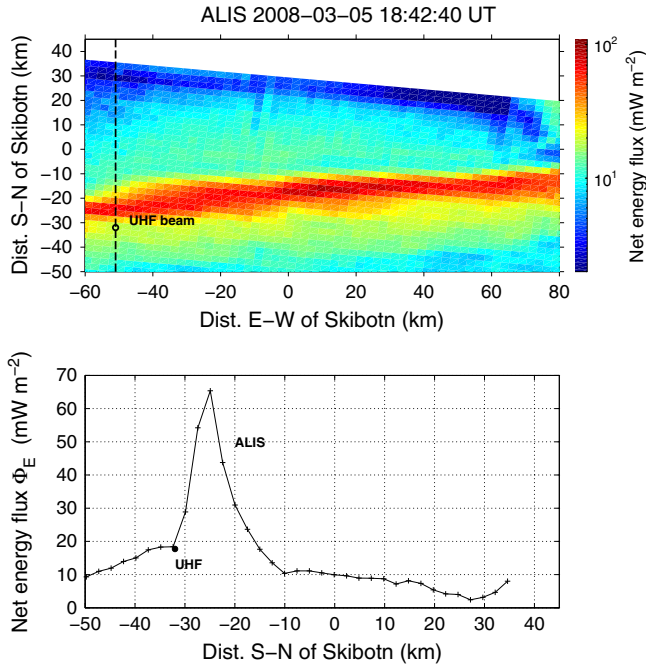


Figure 16. Integrated net energy flux Φ_E in mW m^{-2} at 18:42:40 UT. (top) Map of Φ_E derived from ALIS 2-D reconstructed fluxes over Scandinavia at 260 km altitude. (bottom) Latitudinal cut of the energy flux intersecting the EISCAT plane and along the local magnetic field line. The position of the cut is shown on the top panel by a dashed black line. The integrated energy flux calculated with EISCAT is marked by a black full circle. The white area marks the end of the reconstruction of energy flux due to geometry.

obtained from ALIS (Figure 11). The latitudinal distribution of Φ_E across an arc can be compared to predictions of magnetosphere-ionosphere coupling models [e.g., *Lysak and Dum, 1983; Lysak, 1990; Janhunen and Huuskonen, 1993; Lysak and Song, 2003; Streltsov and Lotko, 2004; Echim et al., 2008*].

5. Perspectives and Conclusions

5.1. Summary

[93] The energy flux of precipitating electrons and its spatial extension above auroral arcs can be estimated by analyzing electron density data sets from incoherent scatter radars and auroral emissions from ground-based imaging systems. In this work, are presented:

[94] 1. A general inversion framework applied to the Auroral Large Imaging System (ALIS) and the European Incoherent Scatter radar (EISCAT) for one coordinated auroral observation taking place in March 2008. The optical inversion is performed in two steps (optical discrete tomography and inversion of emission profile). Radar and optical inversions to estimate electron differential fluxes use an updated common forward model and energy deposition function, described in detail.

[95] 2. A novel generalized technique to determine an accurate initial guess for fast iterative tomographic reconstruction with optical cameras, accounting for

latitudinal/longitudinal and altitudinal intensity variations of the auroral arcs. This technique is preferable to past attempts when determination of the full energy spectrum of precipitating electron is sought.

[96] 3. Two-dimensional energy flux maps with high spatial resolution from the observation of N_2^+ 1NG 4278 Å 3-D volume emission rates with ALIS. The retrieved net energy flux ranged between 60 and 80 mW m^{-2} , with an arc width of 7.5 km. At the location of EISCAT, radar and optical retrievals of precipitation energy fluxes are in excellent agreement. The complex electron fluxes observed suggest that the auroral arc be created by broadband acceleration mechanisms due to dispersive Alfvén waves.

[97] In combination with the high temporal resolution of the EISCAT UHF radar, which may be used for cross calibration, this work constitutes a first step in the study of discrete auroral arcs from the ground and up. Since this method can be applied to the whole time sequence of ALIS images, temporal energy flux maps can be derived to study the evolution of electron precipitation in the formation and brightening of an arc.

5.2. Perspectives

[98] The ALIS-EISCAT campaign of March 2008, supplemented by that of December 2009, contains other events of interest, which will be further explored in coming studies. Future ALIS campaigns will focus on obtaining a better temporal resolution (down to around 5 s) in different geomagnetic conditions and, whenever possible, on obtaining conjugated observations with spacecraft flying at low altitude such as DMSP, in order to investigate how the electron energy flux degrades below 700 km altitude. The ambition with the general method exposed in this article is to start constructing a statistical evolution of precipitated energy fluxes from multi-instrumental ground-based observations. This method should also be easily transposed to other systems of cameras (in or out of the ALIS system).

[99] In connection with a magnetosphere-ionosphere coupling model, the latitudinal distribution of the net energy flux Φ_E along the arc can be used to infer some characteristics of the magnetospheric generator. For example, for inverted-V events, a quasi-static 1-D model such as that of *Echim et al. [2008]* is well-adapted as it provides the net energy flux Φ_E , the field-aligned potential drop ΔV , and the field-aligned current density \mathbf{j}_{\parallel} across the auroral arc for given parameters of the magnetospheric generator. By fine-tuning the predictions of the model with the reconstructed latitudinal distribution of Φ_E , it is then possible to obtain estimates of some of the magnetospheric generator properties, such as electron density and temperature or the altitude of the generator. Moreover, since the height-integrated Pedersen currents \mathbf{J}_P closing the auroral circuit in the ionosphere can be estimated via $\mathbf{j}_{\parallel} = \nabla \cdot \mathbf{J}_P$, the method may be applied along the longitudinal distribution of the arc and a 2-D distribution of \mathbf{J}_P obtained by stacking 1-D solutions along the arc. If values of \mathbf{J}_P significantly change along the arc (longitudinal variations), an additional component due to Hall currents \mathbf{J}_H may also be estimated. This can only be done with 2-D distributions of energy fluxes as provided here by inversion of ALIS data. These applications will be explored in forthcoming papers. Since Figure 15 is more reminiscent of a wave-dominated aurora, inverted-V events will be searched

for in the remaining observations from the 2008 and 2009 coordinated ALIS/EISCAT observational campaigns.

[100] Finally, using 1-D kinetic transport models [e.g., *Sergienko and Ivanov*, 1993; *Lummerzheim and Lilensten*, 1994; *Lilensten and Brelvi*, 2002; *Simon et al.*, 2007], the full structure of the ionosphere, including electron densities and temperatures in the case of kinetic/fluid models such as TRANS4 [*Simon et al.*, 2007], ion composition, auroral emission profiles, or conductivities, may be simulated using the ALIS/EISCAT electron precipitation spectra as input to the models.

Appendix A: Main Results With ALIS

[101] The Auroral Large Imaging System (ALIS) is a unique tool to study the dynamics and the structure of aurora with or without 3-D capabilities. This appendix attempts a historical account of achievements and works performed with ALIS since the first tomographic observation campaigns took place in 1995 [*Aso et al.*, 1998a, 1998b, 2000], in dedication to the work of Prof. Ingrid Sandahl (1949–2011) as Principal Investigator of ALIS.

[102] Tomographic reconstruction of the three-dimensional emission rate of auroral arcs was performed as soon as 1998 by *Frey et al.* [1998] using five CCD cameras to obtain vertical/horizontal distributions of optical auroral emission at the EISCAT site. These reconstructions were used to derive the conductivity from an attempt of calibration between optics and radar measurements. Because of the difficulty of tomography-like reconstruction techniques of the 3-D auroral volume emission rate, specific development to validate and prove the feasibility of the concept with ALIS ensued, resulting in several reference publications of *Gustavsson* [1998, 2000] and *Brändström* [2003]. Inverting 3-D auroral N_2^+ emission rates reconstructed from several ALIS stations, *Gustavsson et al.* [2001a] made the first estimates of the auroral electron spectra and highlighted the potential of such an application to separate spatial and temporal variations in discrete auroral arcs.

[103] From its first light, the ALIS network has also been used for several studies that do not necessarily require 3-D retrieval capabilities, such as artificially enhanced airglow, meteor studies, fluctuations of auroral brightness as a measure of turbulence, black and diffuse aurora, or fine structure of aurora. *Brändström et al.* [1999], *Sergienko et al.* [2000], and *Gustavsson et al.* [2001b, 2002] used ALIS to evidence, validate, and study airglow emission enhancements in different wavelengths following heating and ionospheric HF-pumping experiments with the EISCAT facility. Following *Brändström et al.* [2001], *Pellinen-Wannberg et al.* [2004] later imaged the trails of meteors during the Leonid showers supporting the fact that H_2O^+ may be responsible for discrepancies between observations and modeling. In the study of *Golovchanskaya et al.* [2008], only one station (Skibotn) was used to investigate scaling features of auroral brightness fluctuations, showing that substorm auroral structures exhibit near self-similarity behaviors, with no clear variation with emission line. *Gustavsson et al.* [2008] used for the first time combined EISCAT-ALIS-white light observations to characterize black aurora, which were shown to be consistent with a magnetospheric origin and the partial double loss cone model. *Sergienko et al.* [2008] made

use of three ALIS stations in combination with the satellite FAST particle precipitation data to investigate diffuse aurora and its relation with black aurora. By comparing the results with numerical Monte Carlo simulations, the authors were able to conclude that the diffuse part of the aurora was created by pitch angle diffusion of plasma sheet electrons while the fine structure was the result of higher energy electrons accelerated by whistler mode waves. Recently, *Axelsson et al.* [2012] similarly used five stations with the OI5777 Å filter at high-spatial resolution (500–700 m) to study diffuse auroral structures of about 14 km in width: They concluded that they in turn may originate from stationary mirror mode structures in the magnetospheric equatorial plane. *Safargaleev et al.* [2009] also used the high sensitivity of the ALIS network to characterize electric field enhancements in addition to EISCAT measurements, arguing for interchange instability as the cause of the observed auroral arcs.

[104] In 2008, *Sandahl et al.* [2008], in their review of fine structure of aurora, concluded that there was a need for dedicated campaigns notably with ALIS, and of high spatial and temporal resolution. Following this, *Dahlgren et al.* [2011] presented a multi-instrumental study of energy and flux variations in thin auroral arcs, using the ALIS network as well as the Auroral Structure and Kinetics instrument operated by the University of Southampton. A novel time-dependent inversion method for IS electron densities was also introduced, using the Akaike information criterion [*Akaike*, 1974] on the time-dependent continuity equation to balance the number of free parameters and the accuracy of the fit with the appropriate statistical considerations. The method showed good agreement with optically retrieved electron precipitation spectra. The arcs were found to originate from large electric fields and to be located on boundaries between regions filled with different energy populations of electrons.

[105] Finally, *Tanaka et al.* [2011] made a general contribution to multi-instrumental data sets to build a strategy to exploit in unison existing and future 3-D observatories such as ALIS and the incoming incoherent scatter radar EISCAT_3D in Northern Scandinavia.

[106] **Acknowledgments.** This article is dedicated to Ingrid Sandahl (1949–2011), who was the inspiration and principal investigator of ALIS. She will be deeply missed. C.S.W. also dedicates this paper to his ever-supporting grandmother Marthe M.A. Simon (1909–2012). The authors wish to thank M. Echim and J. De Keyser (BIRA-IASB, Belgium), M. Simon Wedlund (formerly at Otago University, Dunedin, New Zealand), and G. Gronoff (NASA LaRC, VA, USA) for constructive discussions and suggestions. C.S.W. was supported for this project by the Belgian BELSPO-PPS Science Policy through the Action 1 contract MO/35/019 and MO/35/025. H.L. acknowledges the EU funding through the Trans-National Access (TNA) project to perform the observations in March 2008 with the EISCAT facility. The authors also thank Lisa Baddeley for her support during the campaigns. EISCAT is an international association supported by research organizations in China (CRIRP), Finland (SA), Germany (DFG), Japan (NIPR and STEL), Norway (NFR), Sweden (VR), and the United Kingdom (STFC).

[107] Robert Lysak thanks Betty Lanchester and another reviewer for their assistance in evaluating this paper.

References

- Akaike, H. (1974), A new look at the statistical model identification, *IEEE Trans. Autom. Control*, 19(6), 716–723, doi:10.1109/TAC.1974.1100705.
- Alekseeva, G. A., et al. (1996), The Pulkovo spectrophotometric catalog of bright stars in the range from 320 to 1080 nm, *Balt. Astron.*, 5, 603–838.
- Alekseeva, G. A., et al. (1997), The Pulkovo spectrophotometric catalog of bright stars in the range from 320 to 1080 nm - A supplement, *Balt. Astron.*, 6, 481–496.

- Aso, T., M. Ejiri, A. Urashima, H. Miyaoka, Å. Steen, U. Brändström, and B. Gustavsson (1998a), First results of auroral tomography from ALIS-Japan multi-station observations in March, 1995, *Earth Planets Space*, **50**, 81–86.
- Aso, T., M. Ejiri, A. Urashima, H. Miyaoka, Å. Steen, U. Brändström, and B. Gustavsson (1998b), Auroral tomography analysis of a folded arc observed at the ALIS-Japan multi-station campaign on March 26, 1995, in *Proceedings of the NIPR Symposium on Upper Atmosphere Physics, 2nd Symposium on Coordinated Observations of the Ionosphere and the Magnetosphere in the Polar Regions Held 19–20 November, 1996 at NIPR, Tokyo*, vol. 11, edited by S. Okano, pp. 1–10.
- Aso, T., Å. Steen, U. Brändström, B. Gustavsson, A. Urashima, and M. Ejiri (2000), ALIS, a state-of-the-art optical observation network for the exploration of polar atmospheric processes, *Adv. Space Res.*, **26**, 917–924, doi:10.1016/S0273-1177(00)00030-2.
- Axelsson, K., T. Sergienko, H. Nilsson, U. Brändström, Y. Ebihara, K. Asamura, and M. Hirahara (2012), Spatial characteristics of wave-like structures in diffuse aurora obtained using optical observations, *Ann. Geophys.*, **30**(12), 1693–1701, doi:10.5194/angeo-30-1693-2012.
- Barrett, J. L., and P. B. Hays (1976), Spatial distribution of energy deposited in nitrogen by electrons, *J. Chem. Phys.*, **64**, 743–750, doi:10.1063/1.432221.
- Bilitza, D. (2001), International reference ionosphere 2000, *Radio Sci.*, **36**(2), 261–275, doi:10.1029/90JA02125.
- Borovsky, J. E. (1993), Auroral arc thicknesses as predicted by various theories, *J. Geophys. Res.*, **98**, 6101–6138, doi:10.1029/92JA02242.
- Brändström, B. U. E. (2003), The auroral large imaging system—Design, operation and scientific results, *Institutet för rymdfysik (IRF) Sci. Rep.*, 279, IRF, Kiruna, Sweden.
- Brändström, U., T. B. Leyser, Å. Steen, M. T. Rietveld, B. Gustavsson, T. Aso, and M. Ejiri (1999), Unambiguous evidence of HF pump-enhanced airglow, *Geophys. Res. Lett.*, **26**(23), 3561–3564.
- Brändström, U., B. Gustavsson, Å. Steen, and A. Pellinen-Wannberg (2001), ALIS (Auroral Large Imaging System) used for optical observations of the meteor impact process, in *Meteoroids 2001 Conference*, edited by B. Warmbein, pp. 331–336, Eur. Space Agency Spec. Publ., ESA SP-495.
- Brekke, A., C. Hall, and T. L. Hansen (1989), Auroral ionospheric conductances during disturbed conditions, *Ann. Geophys.*, **7**, 269–280.
- Chaston, C. C., C. W. Carlson, J. P. McFadden, R. E. Ergun, and R. J. Strangeway (2007), How important are dispersive Alfvén waves for auroral particle acceleration? *Geophys. Res. Lett.*, **34**, L07101, doi:10.1029/2006GL029144.
- Chiu, Y. T., and J. M. Cornwall (1980), Electrostatic model of a quiet auroral arc, *J. Geophys. Res.*, **85**, 543–556.
- Dahlgren, H., B. Gustavsson, B. S. Lanchester, N. Ivchenko, U. Brändström, D. K. Whiter, T. Sergienko, I. Sandahl, and G. Marklund (2011), Energy and flux variations across thin auroral arcs, *Ann. Geophys.*, **29**, 1699–1712, doi:10.5194/angeo-29-1699-2011.
- De Piero, A. (1991), Multiplicative iterative methods in computed tomography, in *Mathematical Methods in Tomography*, edited by G. Herman, A. Louis, and F. Natterer, pp. 1441–1450, Springer, New York.
- Echim, M. M., M. Roth, and J. de Keyser (2008), Ionospheric feedback effects on the quasi-stationary coupling between LLBL and postnoon/evening discrete auroral arcs, *Ann. Geophys.*, **26**, 913–928, doi:10.5194/angeo-26-913-2008.
- Echim, M. M., R. Maggiolo, M. Roth, and J. De Keyser (2009), A magnetospheric generator driving ion and electron acceleration and electric currents in a discrete auroral arc observed by Cluster and DMSP, *Geophys. Res. Lett.*, **36**, L12111, doi:10.1029/2009GL038343.
- Ellison, D. C., and R. Ramaty (1985), Shock acceleration of electrons and ions in solar flares, *Astrophys. J.*, **298**, 400–408, doi:10.1086/163623.
- Frey, H. U., S. Frey, B. S. Lanchester, and M. Kosch (1998), Optical tomography of the aurora and EISCAT, *Ann. Geophys.*, **16**, 1332–1342, doi:10.1007/s00585-998-1332-y.
- Frey, H. U., et al. (2010), Small and meso-scale properties of a sub-storm onset auroral arc, *J. Geophys. Res.*, **115**, A10209, doi:10.1029/2010JA015537.
- Golovchanskaya, I. V., B. V. Kozelov, T. I. Sergienko, U. Brändström, H. Nilsson, and I. Sandahl (2008), Scaling behavior of auroral luminosity fluctuations observed by Auroral Large Imaging System (ALIS), *J. Geophys. Res. Space Phys.*, **113**, A10303, doi:10.1029/2008JA013217.
- Gull, S. F., and G. J. Daniell (1978), Image reconstruction from incomplete and noisy data, *Nature*, **272**, 686–690, doi:10.1038/272686a0.
- Gustavsson, B. (1998), Tomographic inversion for ALIS noise and resolution, *J. Geophys. Res.*, **103**, 26,621–26,632, doi:10.1029/98JA00678.
- Gustavsson, B. (2000), Three dimensional imaging of aurora and airglow, *Institutet för rymdfysik (IRF) Sci. Rep.*, 267, IRF, Kiruna, Sweden.
- Gustavsson, B., Å. Steen, T. Sergienko, and B. U. E. Brandstrom (2001a), Estimate of auroral electron spectra, the power of ground-based multi-station optical measurements, *Phys. Chem. Earth C*, **26**, 189–194, doi:10.1016/S1464-1917(00)00106-9.
- Gustavsson, B., B. U. E. Brändström, Å. Steen, T. Sergienko, T. B. Leyser, M. T. Rietveld, T. Aso, and M. Ejiri (2002), Nearly simultaneous images of HF-pump enhanced airglow at 6300 Å and 5577 Å, *Geophys. Res. Lett.*, **29**(24), 2220, doi:10.1029/2002GL015350.
- Gustavsson, B., M. J. Kosch, A. Senior, A. J. Kavanagh, B. U. E. Brändström, and E. M. Blixt (2008), Combined EISCAT radar and optical multispectral and tomographic observations of black aurora, *J. Geophys. Res. Space Phys.*, **113**, A06308, doi:10.1029/2007JA012999.
- Gustavsson, B., et al. (2001b), First tomographic estimate of volume distribution of HF-pump enhanced airglow emission, *J. Geophys. Res.*, **106**, 29,105–29,124, doi:10.1029/2000JA900167.
- Haerendel, G., H. U. Frey, C. C. Chaston, O. Amm, L. Juusola, R. Nakamura, E. Seran, and J. M. Weygand (2012), Birth and life of auroral arcs embedded in the evening auroral oval convection: A critical comparison of observations with theory, *J. Geophys. Res.*, **117**, A12220, doi:10.1029/2012JA018128.
- Hedin, A. E. (1991), Extension of the MSIS thermosphere model into the middle and lower atmosphere, *J. Geophys. Res.*, **96**, 1159–1172, doi:10.1029/90JA02125.
- Hoffleit, D., and C. V. Jaschek (1991), *The Bright Star Catalogue*, 5th rev., edited by D. Hoffleit and C. Jaschek, Yale Univ. Obs., New Haven, Conn.
- ICRU Report, (1993), Average energy required to produce an ion pair, *Report No. 31*, International Commission on Radiation Units and Measurements, Washington D.C., USA, 1979, reprinted, ISBN: 0-913394-25-4.
- Janhunen, P. (2001), Reconstruction of electron precipitation characteristics from a set of multiwavelength digital all-sky auroral images, *J. Geophys. Res.*, **106**, 18,505–18,516, doi:10.1029/2000JA000263.
- Janhunen, P., and A. Huuskonen (1993), A numerical ionosphere-magnetosphere coupling model with variable conductivities, *J. Geophys. Res.*, **98**, 9519–9530, doi:10.1029/92JA02973.
- Lilensten, J., and P. L. Blelly (2002), The TEC and F2 parameters as tracers of the ionosphere and thermosphere, *J. Atmos. Sol. Terr. Phys.*, **64**, 775–793, doi:10.1016/S1364-6826(02)00079-2.
- Lummerzhim, D., and J. Lilensten (1994), Electron transport and energy degradation in the ionosphere: Evaluation of the numerical solution, comparison with laboratory experiments and auroral observations, *Ann. Geophys.*, **12**, 1039–1051, doi:10.1007/s00585-994-1039-7.
- Lyons, L. (1981), Discrete aurora as the direct result of an inferred high altitude generating potential distribution, *J. Geophys. Res.*, **86**, 1–8.
- Lysak, R. L. (1990), Electrodynamic coupling of the magnetosphere and ionosphere, *Space Sci. Rev.*, **52**(A4), 33–87, doi:10.1007/BF00704239.
- Lysak, R. L., and C. T. Dum (1983), Dynamics of magnetosphere-ionosphere coupling including turbulent transport, *J. Geophys. Res.*, **88**, 365–380, doi:10.1029/JA088iA01p00365.
- Lysak, R. L., and Y. Song (2003), Kinetic theory of the Alfvén wave acceleration of auroral electrons, *J. Geophys. Res. Space Phys.*, **108**(A4), 8005, doi:10.1029/2002JA009406.
- Marklund, G. T., S. Sadeghi, T. Karlsson, P.-A. Lindqvist, H. Nilsson, C. Forsyth, A. Fazakerley, E. A. Lucek, and J. Pickett (2011a), Altitude distribution of the auroral acceleration potential determined from cluster satellite data at different heights, *Phys. Rev. Lett.*, **106**, 055002, doi:10.1103/PhysRevLett.106.055002.
- Marklund, G. T., et al. (2011b), Evolution in space and time of the quasi-static acceleration potential of inverted-V aurora and its interaction with Alfvénic boundary processes, *J. Geophys. Res.*, **116**, A00K13, doi:10.1029/2011JA016537.
- Mehr, F. J., and M. A. Biondi (1969), Electron temperature dependence of recombination of O_2^+ and N_2^+ ions with electrons, *Phys. Rev.*, **181**, 264–271, doi:10.1103/PhysRev.181.264.
- Newell, P. T., T. Sotirelis, and S. Wing (2009), Diffuse, monoenergetic, and broadband aurora: The global precipitation budget, *J. Geophys. Res.*, **114**, A09207, doi:10.1029/2009JA014326.
- Nygrén, T., M. Markkanen, M. Lehtinen, and K. Kaila (1996), Application of stochastic inversion in auroral tomography, *Ann. Geophys.*, **14**(11), 1124–1133, doi:10.1007/s00585-996-1124-1.
- Osepian, A., and S. Kirkwood (1996), High-energy electron fluxes derived from EISCAT electron density profiles, *J. Atmos. Terr. Phys.*, **58**, 479–487.
- Partamies, N., P. Janhunen, K. Kauristie, S. Mäkinen, and T. Sergienko (2004), Testing an inversion method for estimating electron energy fluxes from all-sky camera images, *Ann. Geophys.*, **22**, 1961–1971, doi:10.5194/angeo-22-1961-2004.
- Pellinen-Wannberg, A., E. Murad, B. Gustavsson, U. Brändström, C.-F. Enell, C. Roth, I. P. Williams, and Å. Steen (2004), Optical observa-

- tions of water in Leonid meteor trails, *Geophys. Res. Lett.*, *31*, L03812, doi:10.1029/2003GL018785.
- Picone, J. M., A. E. Hedin, D. P. Drob, and A. C. Aikin (2002), NRLMSISE-00 empirical model of the atmosphere: Statistical comparisons and scientific issues, *J. Geophys. Res.*, *107*(A12), 1468, doi:10.1029/2002JA009430.
- Rees, M. H. (1963), Auroral ionization and excitation by incident energetic electrons, *Planet. Space Sci.*, *11*, 1209–1218, doi:10.1016/0032-0633(63)90252-6.
- Rees, M. H. (1989), *Physics and Chemistry of the Upper Atmosphere*, 297 pp., Cambridge Univ. Press, Cambridge, U. K.
- Rees, M. H., and D. Luckey (1974), Auroral electron energy derived from ratio of spectroscopic emissions. I - Model computations, *J. Geophys. Res.*, *79*, 5181–5186, doi:10.1029/JA079i034p05181.
- Rydesäter, P., and B. Gustavsson (2000), Investigation of smooth basis functions and an approximated projection algorithm for faster tomography, *Int. J. Imaging Syst. Technol.*, *11*(6), 347–354, doi:10.1002/ima.1019.
- Safargaleev, V. V., T. I. Sergienko, A. E. Kozlovsky, I. Sandahl, U. Brändström, and D. N. Shibaeva (2009), Electric field enhancement in an auroral arc according to the simultaneous radar (EISCAT) and optical (ALIS) observations, *Geomagn. Aeron.*, *49*, 353–367, doi:10.1134/S0016793209030098.
- Sandahl, I., T. Sergienko, and U. Brändström (2008), Fine structure of optical aurora, *J. Atmos. Sol. Terr. Phys.*, *70*, 2275–2292, doi:10.1016/j.jastp.2008.08.016.
- Semeter, J., and F. Kamalabadi (2005), Determination of primary electron spectra from incoherent scatter radar measurements of the auroral E region, *Radio Sci.*, *40*, RS2006, doi:10.1029/2004RS003042.
- Semeter, J., M. Mendillo, and J. Baumgardner (1999), Multispectral tomographic imaging of the midlatitude aurora, *J. Geophys. Res.*, *104*, 24,565–24,586, doi:10.1029/1999JA900305.
- Sergienko, T., B. Gustavsson, Å. Steen, U. Brändström, M. Rietveld, T. B. Leyser, and F. Honary (2000), Analysis of excitation of the 630.0 nm airglow during a heating experiment in Tromsø on February 16, 1999, *Phys. Chem. Earth Part B Hydrol. Oceans Atmos.*, *25*(5-6), 531–535.
- Sergienko, T., I. Sandahl, B. Gustavsson, L. Andersson, U. Brändström, and Å. Steen (2008), A study of fine structure of diffuse aurora with ALIS-FAST measurements, *Ann. Geophys.*, *26*, 3185–3195, doi:10.5194/angeo-26-3185-2008.
- Sergienko, T., B. Gustavsson, U. Brändström, and K. Axelsson (2012), Modelling of optical emissions enhanced by the HF pumping of the ionospheric F-region, *Ann. Geophys.*, *30*, 885–895, doi:10.5194/angeo-30-885-2012.
- Sergienko, T. I., and V. E. Ivanov (1991), Transport of electrons in atmospheric gases. I - Integral characteristics, *Geomagn. Aeron.*, *31*, 635–642.
- Sergienko, T. I., and V. E. Ivanov (1993), A new approach to calculate the excitation of atmospheric gases by auroral electron impact, *Ann. Geophys.*, *11*, 717–727.
- Sheehan, C. H., and J.-P. St.-Maurice (2004), Dissociative recombination of N_2^+ , O_2^+ , and NO^+ : Rate coefficients for ground state and vibrationally excited ions, *J. Geophys. Res.*, *109*, A03302, doi:10.1029/2003JA010132.
- Simon, C., J. Liliensten, J. Moen, J. M. Holmes, Y. Ogawa, K. Oksavik, and W. F. Denig (2007), TRANS4: A new coupled electron/proton transport code - Comparison to observations above Svalbard using ESR, DMSP and optical measurements, *Ann. Geophys.*, *25*, 661–673, doi:10.5194/angeo-25-661-2007.
- Simon Wedlund, C., G. Gronoff, J. Liliensten, H. Ménager, and M. Barthélemy (2011), Comprehensive calculation of the energy per ion pair or W values for five major planetary upper atmospheres, *Ann. Geophys.*, *29*, 187–195, doi:10.5194/angeo-29-187-2011.
- Streltsov, A. V., and W. Lotko (2004), Multiscale electrodynamics of the ionosphere-magnetosphere system, *J. Geophys. Res.*, *109*, A09214, doi:10.1029/2004JA010457.
- Tanaka, Y.-M., et al. (2011), Feasibility study on generalized-aurora computed tomography, *Ann. Geophys.*, *29*, 551–562, doi:10.5194/angeo-29-551-2011.
- Torr, M. R., J.-P. St.-Maurice, and D. G. Torr (1977), The rate coefficient for the $O^+ + N_2$ reaction in the ionosphere, *J. Geophys. Res.*, *82*(22), 3287–3290, doi:10.1029/JA082i022p03287.
- Vaivads, A., et al. (2003), What high altitude observations tell us about the auroral acceleration: A Cluster/DMSP conjunction, *Geophys. Res. Lett.*, *30*(3), 1106, doi:10.1029/2002GL016006.
- Vondrak, R. R., and A. Baron (1977), A method of obtaining the energy distribution of auroral electrons from incoherent scatter radar measurements, in *Radar Probing of the Auroral Plasma: Proceeding of the EISCAT Summer School, Tromsø, June 5–13, 1975*, edited by A. Brekke, pp. 315–330, Univ. Ets forlaget, Oslo.
- Vondrak, R. R., and R. D. Sears (1978), Comparison of incoherent scatter radar and photometric measurements of the energy distribution of auroral electrons, *J. Geophys. Res.*, *83*, 1665–1667, doi:10.1029/JA083iA04p01665.
- Walls, F. L., and G. H. Dunn (1974), Measurement of total cross sections for electron recombination with NO^+ and O_2^+ using ion storage techniques, *J. Geophys. Res.*, *79*, 1911–1915, doi:10.1029/JA079i013p01911.